Fixation of CO_2 by chrysotile in low-pressure dry and moist carbonation: Ex-situ and in-situ characterizations

Faïçal Larachi [a,*], Insaf Daldoul [a], Georges Beaudoin [b]

[a] *Department of Chemical Engineering, Laval University, 1065, Avenue de la Médecine, Québec, QC, Canada G1V 0A6*
[b] *Department of Geology and Geological Engineering, Laval University, 1065, Avenue de la Médecine, Québec, QC, Canada G1V 0A6*

Abstract

A detailed study of low-pressure gas–solid carbonation of chrysotile in dry and humid environments has been carried out. The evolving structure of chrysotile and its reactivity as a function of temperature (300–1200 °C), humidity (0–10 mol %) and CO_2 partial pressure (20–67 mol %), thermal preconditioning, and alkali metal doping (Li, Na, K, Cs) have been monitored through in-situ X-ray photoelectron spectroscopy, isothermal thermogravimetry/mass spectrometry, ex-situ X-ray powder diffraction, and water and nitrogen adsorption/desorption. Based on chrysotile crystalline structure and its nanofibrilar orderliness, a multistep carbonation mechanism was elaborated to explain the role of water during chrysotile partial amorphisation, formation of periclase, brucite, and hydromagnesite crystalline phases, and surface passivation thereof, during humid carbonation. The weak carbonation reactivity was rationalized in terms of incongruent CO_2 van der Waals molecular diameters with the octahedral–tetrahedral lattice constants of chrysotile. This lack of reactivity appeared to be relatively indifferent to the facilitated water crisscrossing during chrysotile core dehydroxylation/pseudo-amorphisation and surface hydroxylation induced product stabilization during humid carbonation. Thermodynamic stability domains of the species observed at low pressure have been thoroughly discussed on the basis of X-ray powder diffraction patterns and X-ray photoelectron spectroscopy evidence. The highest carbon dioxide uptake occurred at 375 °C in moist atmospheres. On the basis of chrysotile fresh N_2 BET area, nearly 15 atoms out of 100 of the surface chrysotile *brucitic* Mg moiety have been carbonated at this temperature which was tantamount to the carbonation of about 2.5 at. % of the total brucitic Mg moiety in chrysotile. The carbonation of brucite $(Mg(OH)_2)$ impurities coexisting in chrysotile was minor and estimated to contribute by less than 17.6 at. % of the total converted magnesium. The presence of cesium traces (3 Cs atoms per 100 Mg atoms) was found to boost chrysotile carbonation capacity by a factor 2.7.

1. INTRODUCTION

The potential link between adverse global phenomena and anthropogenically caused increases in greenhouse gas levels in the atmosphere is driving exploration of various technologies to mitigate the release of carbon dioxide and other gases. Emitted in large proportions, especially from (stationary) fossil-fuel based power plants, carbon dioxide is recognized as a major greenhouse gas. This has turned CO_2 capture and sequestration (CCS) into an extensively investigated topic (Bernstein et al., 2007).

Carbonation approaches, proposed by Seifritz (1990) and then advocated by Lackner and coworkers (Lackner et al., 1995, 1997), consists in enabling above-ground ex-situ CCS processes by taking advantage of already available ores, mining tailings and wastes, especially those consisting of mafic/ultramafic igneous rocks due to their high Mg content. This approach still faces investigation regarding its engineering feasibility or economic viability within the context of mitigation of greenhouse gas emissions. The appeal for the magnesium rich minerals stems from their large-

* Corresponding author. Tel.: +1 (418) 656 3566; fax: +1 (418) 656 5993.
  E-mail address: Faical.Larachi@gch.ulaval.ca (F. Larachi).

scale availability, which, in stoichiometric perspective, are among the few realistic options which can buffer CO_2 gaseous emissions within the fossil-fuel driven economic paradigm. The other motive is that valence II Mg, bound within a silicate matrix in these naturally-occurring minerals as oxyhydroxides (serpentine) or oxides (pyroxene, olivine), is reactive vis-à-vis CO_2 (Gerdemann et al., 2007; Dufaud et al., 2009). A last motive is the stability of the magnesite-like products, measurable through several-millennium time-scale (Lackner, 2003) and without significant environmental impacts.

Serpentine, olivine, and pyroxene, as magnesium donor silicates, are under intense academic and industrial scrutiny as cheap and abundant CCS raw materials, and where, broadly speaking, four philosophical lines of thought are being envisaged regarding the way magnesium silicates are to be carbonated:

(i) In-situ geological storage takes advantage of the high-pressure/high-temperature hydrothermal environments prevailing underground to allow CO_2 mineral trapping using olivine (forsterite), pyroxene, and serpentine (Giammar et al., 2005; Dufaud et al., 2009); while the operating conditions are not controllable at will, only site selection is left as the major degree of freedom for a CCS implementation.

(ii) Ex-situ sequestration as high-pressure/high-temperature aqueous (or wet) single/multistep carbonation chemistries involving leaching and dissolution of serpentine and subsequent precipitation of magnesium carbonate using as a substrate olivine (O'Connor et al., 2002; Park and Fan, 2004; Béarat et al., 2006; Gerdemann et al., 2007), and serpentine polymorphs: lizardite (McKelvy et al., 2004; Schulze et al., 2004; Gerdemann et al., 2007), and antigorite (Marato-Valer et al., 2005; Gerdemann et al., 2007; Krevor and Lackner, 2009).

(iii) Ex-situ sequestration as high-pressure/high-temperature gas–solid carbonation of antigorite/lizardite/chrysotile natural mixtures (Zevenhoven and Kohlmann, 2001; Zevenhoven et al., 2006; Fagerlund et al., 2009).

(iv) Ex-situ sequestration as low-pressure/high-temperature indirect gas–solid carbonation subsequent to wet magnesium extraction (Lin et al., 2008) or dry MgO liberation (Zevenhoven et al., 2008) or low-temperature wet all-through hydromagnesite production from serpentinite (Teir et al., 2009).

Apart from the Albany Research Center which studied the aqueous carbonation of chrysotile-containing serpentine extensively (O'Connor et al., 2002, 2005), open-literature studies on chrysotile, the asbestiform polymorph of serpentine, destined for ex-situ above-ground CCS processes are to the best of our knowledge, rare. Chrysotile mining and milling residue heaps in southern Québec (Canada) are estimated to be about 2 billion tons (metric) and may constitute a regional low-cost source for potential CCS. Previous research has shown that spontaneous carbonation at weathering conditions forms hydromagnesite

within chrysotile residues in southern Québec (Huot et al., 2003) and at Balangero in Italy (Beaudoin et al., 2008) whereas nesquehonite, dypingite and lansfordite are found in chrysotile mining waste from Cassiar and Clinton Creek, respectively, in British Columbia and Yukon, Canada (Wilson et al., 2009). The spontaneous mineral carbonation of chrysotile milling residue from atmospheric CO_2 is akin to crustal weathering and its role is major in buffering atmospheric CO_2 concentration over geological periods (Berner and Kothavala, 2001). It is accelerated by the increased surface area and high porosity of milled residue. Spontaneous mineral carbonation of mining waste, however, remains very slow for direct industrial implementation but can be tremendously enhanced through elevated temperatures and/or pressures. The enthalpy of chrysotile carbonation is $-35 \, kJ/mol_{CO_2}$ (Lackner et al., 1995). Despite the fact that this is more than a factor of two smaller than values for pyroxene or forsterite, respectively, -81 and $-88 \, kJ/mol_{CO_2}$ (Lackner et al., 1995), the exothermic mineral carbonation of chrysotile could result, if integrated efficiently, in a disposal process that is net energy producer, which, along with valuing other metals, such as nickel, present in chrysotile tailings, could yield an economically viable above-ground sequestration process for retrofit on existing, or for new, CO_2 emitting industries.

This work reports on systematic low-pressure gas–solid carbonation studies of chrysotile, with as a chief objective an understanding of the chemistry at work in dry and moist environments as well as the evolution of chrysotile structure and its carbonation by and end-products as a function of temperature, moisture, and its wear and tear under carbonation/calcination cycles. To elaborate on chrysotile carbonation reactivity, an in-situ surface study following carbonation/calcination under controlled atmospheres has been carried out in parallel with thermogravimetric analyses. Results on the stimulation of CO_2 fixation on chrysotile via impregnation with alkali metals and chrysotile thermal treatments were also addressed as well as an analysis of the thermodynamic stability fields of the observed phases on the basis of X-ray powder diffraction patterns and X-ray photoelectron spectroscopy.

2. CHRYSOTILE STRUCTURE, SOME BACKGROUNDS

Chrysotile ($Mg_3Si_2O_5(OH)_4$) is a nanotubular (1:1 layer) hydrous phyllosilicate formed during the hydration of mafic/ultramafic rocks by hydrothermal fluids at temperatures lower than 350 °C (Auzende et al., 2004; Evans, 2004). This magnesium hydroxide silicate exhibits a scroll-like bilayer consisting of a **t**etrahedral $[SiO_4]^{4-}$ silicate sheet (**T**) "spreading" along the surface of mutual contact with a tri**o**ctahedral $[Mg_3O_2(OH)_4]^{2-}$ brucite-like sheet (**O**). Chrysotile is a polymorph of serpentine in which the **T**–**O** sheet lateral misfit is accommodated, to a degree, by a change in curvature resulting in various curved crystal shapes and sizes (Krinari and Khalitov, 1995; Evans, 2004) such as the curled (often uncapped) cylindrical structures, of which a transverse slice along the nanofibril axis is drawn in Fig. 1a.
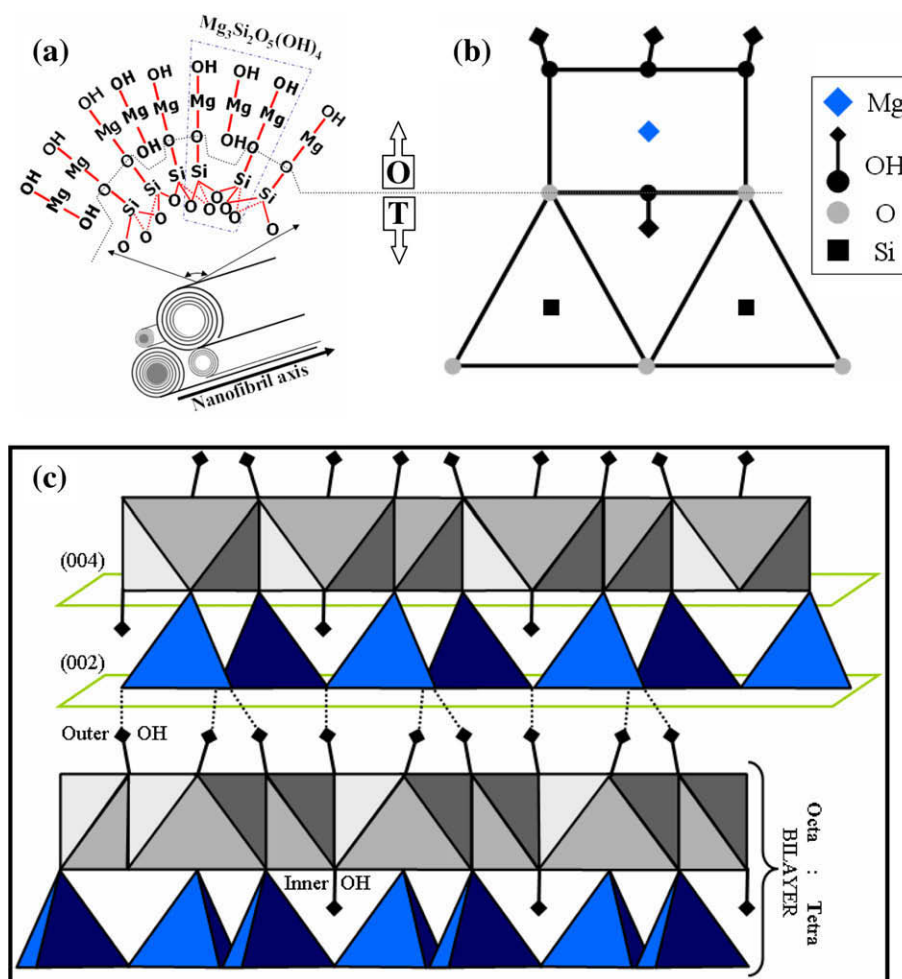
Fig. 1. (a) Curled cylindrical stacking of chrysotile magnesium hydroxide silicate ($Mg_3Si_2O_5(OH)_4$) and corresponding **T–O** structure (after Turci et al., 2008). (b) Trioctahedral sheet silicate illustrating substitution of two hydroxide from brucite by two apical oxygens of the tetrahedral silicate to generate the serpentine mineral structure. (c) Schematic rendering of the crystal structure of chrysotile highlighting planes (0 0 2) and (0 0 4) (after Turci et al., 2008).

The chrysotile stacked cylindrical lamellas are organized such that the Si- and Mg-bearing sheets point, respectively, inwards and outwards. This configuration is not without consequences for CO_2 incorporation into the chrysotile lattice and on Mg carbonation reactivity. Crosswise thickness of naturally-occurring chrysotile nanofibrils is limited by curvature-induced intra-layer strains which yield nanofibrils with an average diameter as large as 40 nm (Evans, 2004). The intra-layer strain is minimal for a radius of curvature of about 8.8 nm which implies chrysotile nanofibrils in nature must grow hollow (inner diameter about 3.5 nm). The chrysotile bilayer is rigidly "bolted", from within, via two apical oxygen issued from as many vicinal $[SiO_4]^{4-}$ tetrahedra of the unit cell which are covalently bonded to the two octahedral Mg of the O—Si—O—**Mg**—OH moieties (Fig. 1b). These two Mg atoms will be referred to as *lateral* Mg. The third (or *core*) Mg, with brucitic inheritance (HO—**Mg**—OH), is intercalated in-between according to an azimuthal periodicity and does not chemically bond to the silica layer (Fig. 1a). Its innermost hydroxyl group is embedded at the center of the pseudo-hexagonal Si network

contributing solely to intra-bilayer van der Waals interactions with the adjacent Si-centered tetrahedral oxygens (Fig. 1b and c). The three outermost hydroxyl groups, on the contrary, allow inter-bilayer van der Waals **T–O**··**T–O** links between the octahedral sheet of one bilayer and the tetrahedral sheet of a nearby bilayer (Fig. 1c) resulting in the naturally-occurring bundles of closely packed parallel nanofibrils (Liu et al., 2007).

3. EXPERIMENTAL

3.1. Chrysotile sorbents

Chrysotile, originating from Thetford Mines, Québec, with certified purity between 90 and 95 wt% (classification: 9-UN 2590-PG III-RG US-EPA: A-152-4672) was supplied by Lab Chrysotile Canada. The major polytype originating from these mines is clinochrysotile (Whittaker, 1956a). The Québec deposits are practically deprived of the *ortho*-chrysotile polytype while a marginal portion of the Thetford Mines chrysotile specimens would be of a *para*-chrysotile

polytype (Whittaker, 1956b,c). The received native white and fluffy-looking fibrous chrysotile mineral samples were sieved to isolate the 37–75 μm fraction (400–200 mesh Tyler sieves) studied here and which will henceforth be referred to as "raw chrysotile".

Chrysotile modified sorbents doped with lithium, sodium, potassium, and cesium oxides were synthesized by wet impregnation using the corresponding Li, Na, K, and Cs nitrate precursors (Sigma–Aldrich) according to a protocol close to that of Reddy and Smirniotis (2004). The promoted sorbents were obtained by dissolving the appropriate amount of nitrate precursors in a dilute aqueous chrysotile slurry. The modified sorbents had a 10 wt% X/MgO mass ratio (X = Cs, K, Na, or Li) or equivalently, 0.03 (Cs), 0.10 (K), 0.18 (Na), and 0.58 (Li) atom X/atom Mg. Two grams of raw chrysotile (about 0.8 g MgO), slurried in 160 mL de-ionized water, were mixed for 2 h at ambient conditions with the required mass of alkali nitrate. The suspension was then heated under mixing until water had completely evaporated. The collected solid residue was dried overnight at 125 °C, and subsequently calcined under helium for 4 h at 400 °C. This temperature was low enough to prevent meaningful dehydroxylation of chrysotile (Cattaneo et al., 2003).

Commercial powders of periclase (30 mesh, 17 m²/g), anhydrous silica (9–13 μm, 220 m²/g), anhydrous dicesium monoxide, and anhydrous magnesium carbonate, all from Sigma–Aldrich, were procured for assessing the carbonation response of chrysotile and for analyzing the binding energy shifts during the X-ray photoelectron spectroscopic studies.

3.2. Analytical techniques

3.2.1. Ex-situ X-ray powder diffraction analysis

Ex-situ phase identification of the crystalline phases of the samples, taken before and after TGA treatments, was made possible from X-ray powder diffraction (XRPD) patterns registered on a Siemens D5000 X-ray powder diffractometer using a Cu K$_\alpha$ radiation ($\lambda = 1.54059$ Å) generated at 40 kV and an emission current of 30 mA. A $\Delta\theta$ scanning rate of 1°/min over the 5–65° scattering angle scan range with a step size of 0.04° and 1.2 s count time were typically applied. The observed diffraction peaks were compared with respect to those reported in the Joint Committee on Powder Diffraction Standards repository: chrysotile, periclase, brucite, hydromagnesite, magnesite, forsterite (olivine), enstatite (pyroxene), cesium oxide, and magnetite.

3.2.2. X-ray fluorescence analysis

Elemental analysis of the raw chrysotile was obtained through X-ray fluorescence (XRF) after fusion in lithium borate of about 2 g of the mineral samples. Raw chrysotile constitutive analytes and their standard deviations are provided in Table 1. Na was below detection limits, while the major elemental contaminations, such as Fe and Al, would suggest partial substitutions with structural Mg and Si (Auzende et al., 2004). Minority elemental contaminations, i.e., Ca, K, Cr, Ti, Mn, and P, were also quantified or detected. The computed atomic ratio Mg/Si = 1.525 slightly

Table 1
wt% of analytes constitutive of Thetford mines (Québec) raw chrysotile.

Analyte	wt%
SiO_2	38.5 ± 0.2
MgO	39.4 ± 0.1
Al_2O_3	0.86 ± 0.01
Fe_2O_3	4.9
CaO	0.16
K_2O	0.16
Cr_2O_3	0.09
TiO_2	0.01
MnO	0.06
P_2O_5	0.01
LOI[a]	14.4
Total	98.4 ± 0.3

[a] Lost on ignition.

exceeds the theoretical chrysotile stoichiometric ratio leaning towards native chrysotile possibly containing excess Mg-bearing minerals, presumably as an extra-framework brucite (see Fig. EA-1-1, Electronic annex EA-1). On the basis of $Mg_3Si_2O_5(OH)_4$ and $Mg(OH)_2$ stoichiometric formulae and aided with Table 1 composition, it was found that 90.2 wt% of the raw mineral matrix would be assigned to chrysotile and about 6.7 mg/g sample as brucite. It is estimated that 12 out of 10^3 magnesium atoms in the mineral belong to brucite. However, no independent direct acid-leach tests were attempted to confirm the proportion of brucite in the inferred mineralogy. The computed Al/Si and Fe/Mg atomic substitution ratios based on chrysotile ideal composition are, respectively, 0.026 and 0.063. However, the Ca/Si and K/Si atomic ratios, respectively, 0.0044 and 0.0052 require much lower Al and Si intra-framework substitutions to satisfy electro-neutrality in the phyllosilicate trioctahedral structure. Therefore, it is plausible that a majority of Fe and Al are in the form of extra-framework iron oxide and alumina which contribute to close the mass balance of the raw chrysotile samples (see Table 1). As shown in Fig. EA-1-1, magnetite (FeII/FeIII = ½) was identified as the third XRPD most abundant, and only crystalline, iron-oxide phase that would account for this extra-framework iron.

3.2.3. Tandem thermogravimetric analysis–mass spectrometry

A thermogravimetric analyzer (Perkin Elmer Lab System Diamond TGA-DTA) coupled with a mass spectrometer with quadrupole analyzer (Thermostar Prisma QMS200, Pfeiffer Vacuum) were used for monitoring the water and CO_2 uptake/release in prograde and isothermal heating, and during carbonation/calcination temperature swings. The TGA (thermogravimetry analyzer) reaction chamber was continuously purged by He/N_2 gas to prevent backflow of the gaseous species into the TGA electronic part. The weight percent loss/gain of the sample and temperature were registered along with the positive ion currents, stemming from the molecular ions H_2O^+ ($m/z = 18$) and CO_2^+ ($m/z = 44$), which were monitored via quadrupole mass spectrometry (QMS). Typically, about 25 mg samples were

contained in platinum or ceramic crucibles. Weight percentage errors were better than 0.04% (10 μg/25 mg). Prior to TGA tests, the samples were submitted to heat pretreatment for 12 h at 150–200 °C for removing physisorbed water and other pre-adsorbed gases. During calcination, each sorbent was exposed to prograde heating at 5 °C/min under He (50 NmL/min) + N_2 (100 NmL/min) and held for 3 h at calcination temperatures (300, 500, 600, 700, 900, 1200 °C) before resuming a gentle quench at 10 °C/min down to ambient temperature. During dry carbonation, the sample was heated at 5 °C/min under He (50 NmL/min) + N_2 (100 NmL/min) and maintained at target temperature until the measured mass virtually stabilized. Then gas flow was switched to CO_2 (100 NmL/min) + He (50 NmL/min) for isothermal carbonation until subsequent sample mass stabilization. Moist carbonation tests were run according to a similar protocol by sweeping 100 NmL/min (CO_2 + H_2O) stream with variable composition. During carbonations, the isothermal temperatures were varied between 150 and 1200 °C, followed by gentle quenches after reaction completion at 10 °C/min. The CO_2 mole fractions were varied between 20% and 67%, and water moisture mole fractions from 0% to 10%. The mass percentage expressing the changes in g per g of sample is denoted by W, e.g., W_{H_2O} and $W_{CO_2+H_2O}$ are water uptake and total mass uptake in moist carbonation, respectively.

3.2.4. Nitrogen adsorption/desorption

Raw and alkali-metal-doped chrysotile samples, in the fresh state, and post-calcination and post-carbonation were characterized ex-situ for the evolution of their textural properties at different temperatures and gas composition environments in the TGA tests. The specific surface areas, and pore volumes and sizes were determined using N_2 adsorption/desorption analyses cast through the BET (Brunauer–Emmett–Teller) model and BJH (Barrett–Joyner–Halenda) porometry. N_2 adsorption isotherms at 77 K were measured on a Micromeritics TRISTAR 3000 at residual pressures down to about 10^{-5} Torr.

The N_2 BET specific surface area measured for raw chrysotile is $SSA_{BET} = 14.4 \text{ m}^2/\text{g}$. This is ca. 30% less than the value reported by Candella et al. (2007) in their study of Québec chrysotile. However, our measured BET surface area is triple the one reported by Park and Fan (2004) for a Pennsylvania mined serpentine, identified as "olivine", according to the U.S. topotaxonomy shown by Gerdemann et al. (2007). The raw chrysotile BJH average pore diameter is 5.5 nm and compares pretty well with the Brazilian chrysotile from Uruaçu Mines (Gollmann et al., 2008, 2009).

3.2.5. X-ray photoelectron spectroscopy

The X-ray photoelectron spectra were acquired at room temperature on an AXIS ULTRA X-ray photoelectron spectrometer from Kratos Analytical using Mg K_α ($hv = 1253.6$ eV) (or when necessary, Al K_α ($hv = 1486.6$ eV)) monochromatic X-ray sources. The background pressure in the spectrometer analyzing chamber was kept below 7.5×10^{-8} Torr. This chamber is hyphenated to a reaction chamber in which wafers of the chrysotile-bearing samples were carbonated/calcined in-situ at atmospheric pressure

and immediately thereafter moved into the analyzing chamber for surface analysis. This precaution precluded exposure to or contamination by, atmospheric interfering contaminants of the sample surfaces during sample manipulation. To prevent accidental dispersion of the material in the reaction chamber, the powdered raw chrysotile and 10% Cs-doped chrysotile were wafered as 1 cm diameter and 3 mm thick discs. The wafers were sensed by the X-ray source operated at ca. 300 W. The photoelectron kinetic energies were measured using a hemispherical analyzer working in a constant pass energy mode. Survey scans (0–1150 eV) and high-resolution spectra on C 1s, O 1s, Mg 2p, Si 2p, and Cs 3d were acquired with nominal resolutions of 1 and 0.1 eV, respectively.

The reaction chamber was connected to CO_2 and N_2 gas cylinders (Praxair) and a steam generator. The connecting tubes were heated to prevent condensation of water while in transit to the Kratos reaction chamber. Three controlled-atmosphere surface state interrogations were performed in the XPS assembly on raw chrysotile and 10%Cs-doped chrysotile: step (1) pre-reaction fresh mineral per se, step (2) post-carbonation, step (3) post-calcination of the mineral carbonated in step (2). During step (2) sample heat-up was carried out in N_2 atmosphere at 100 NmL/min until a temperature of 375 °C was attained. Nitrogen flow was permuted with a 90 NmL/min CO_2 + 10 NmL/min H_2O flow and carbonation was maintained for 10 h. The sample was afterwards moved to the analyzing chamber for XPS analysis and then brought back to the reaction chamber where calcination (step (3)) was immediately resumed under 100 NmL/min N_2 flow at 500 °C for 6 h. The sample was moved back into the analyzing chamber for an ultimate surface analysis after the CO_2 fixated in step (2) would have theoretically been freed.

Also, the commercial powders of MgO, $MgCO_3$, SiO_2, Cs_2O, were analyzed in the powdered state through XPS in the as-received state, and post-carbonation at 375 °C under 90 NmL/min CO_2 + 10 NmL/min H_2O + 50 NmL He, and post-calcination at 500 °C under 100 NmL/min N_2 + 50 NmL He in the TGA system.

To correct for the charge effects occurring during the XPS analyses of the (poorly conducting) chrysotile samples, the binding energy of the C 1s core level from adventitious carbon at 285 ± 0.1 eV was used as a reference to calibrate the high-resolution spectra (Piché and Larachi, 2005). The recorded spectra were decomposed by curve fitting synthetic peak components using the software package Casa-XPS1 (computer aided surface analysis for X-ray photoelectron spectroscopy; Casa Software, UK) by means of symmetric Gaussian–Lorentzian mixed peak shapes to approximate the line shapes of the C 1s core level spectra. Peak synthesis was performed after Shirley background subtraction.

4. RESULTS AND DISCUSSION

4.1. In-situ characterization

Because of its ability to sense chemical environments over depths up to 10 nm, XPS is particularly useful to sense

the chemical evolution of chrysotile during carbonation, especially in low-conversion conditions as obtained in our low-pressure study. XPS would capture surface signals averaged over about 10 unit cells given the chrysotile lattice constants.

A summary for the C 1s, O 1s, Mg 2p, Si 2p, and Cs $3d_{5/2}$ core electrons' high-resolution spectra is given in Table 2 in terms of binding energy (BE) shift, peak full width at half-maximum, and chemical environment assignment. Peak assignments were resolved through information previously given by Hamoudi et al. (1999), Larachi et al. (2004), via the NIST X-ray photoelectron spectroscopy database (Wagner et al., 2007), and when possible by analogy with FTIR assignments regarding the C 1s assignments (Evans and Whateley, 1967; Philipp and Fujimoto, 1992). Figs. 2–4 and those presented in Electronic annex EA-1 illustrate the core level spectra for C 1s, Mg 2p, Cs $3d_{5/2}$, Si 2p (Fig. EA-1-4), and O 1s (Fig. EA-1-5).

Fig. 2 features the C 1s core electrons' high resolution XP spectra for post-calcined commercial periclase, commercial magnesite, raw chrysotile (pre-reaction fresh, step (1)), raw Cs-doped chrysotile (pre-reaction fresh, step (1)), carbonated Cs-doped chrysotile (step (2)), and calcined Cs-doped chrysotile (step (3)), see XPS instrumental section above.

The C—$\underline{C}$—C and/or $\underline{C}$—H components, at BE ≈ 285 eV, appear on all five samples regardless of the environment to which chrysotile was exposed to. They were followed in the order of increasing BEs by the unidentate species, M—(O—)$_3\underline{C}$ (u), near BE ≈ 286.3 eV, the $\underline{br}$idging carbonate species, (MO—)$_2\underline{C}$=O (br), at BE ≈ 287.5 eV, the $\underline{bi}$dentate carbonate species, M(—O—)$_2\underline{C}$=O (bi), at BE ≈ 289.3 eV, and the surface carbonate species, CO_3^{2-}, at BE = 290.3 eV as determined for commercial $MgCO_3$ and carbonated chrysotile. Also, surface bicarbonate species, MO—$\underline{C}$(OH)=O, with BE between that of br and bi are

Table 2
XP spectra fit assessment for C 1s, O 1s, Mg 2p, Si 2p, and Cs 3d core electrons with peak assignments for raw and doped chrysotile, fresh, calcined, and carbonated with comparison to a commercial magnesium carbonate.

	Core electron		Assignment[b]	Peak position (eV)	FWHM[a] (eV)
Raw chrysotile	C 1s	▼	C—$\underline{C}$—C, $\underline{C}$—H	285.1	2.2
			(MO—)$_2\underline{C}$=O (br)	287.4	2.2
			M(—O—)$_2\underline{C}$=O bi	289.6	2.2
	O 1s			531.8	2.3
	Mg 2p			49.8	1.8
	Si 2p			102.7	2.1
10% Cs-doped chrysotile	C 1s	▼	C—$\underline{C}$—C, $\underline{C}$—H	285.0	2.0
			(MO—)$_2\underline{C}$=O (br)	287.4	2.0
			M(—O—)$_2\underline{C}$=O bi	289.3	2.0
	O 1s			531.4	2.5
	Mg 2p			49.7	1.9
	Si 2p			102.7	2.2
	Cs 3d			725.0	2.2
Calcined 10% Cs-doped chrysotile	C 1s	▼	C—$\underline{C}$—C, $\underline{C}$—H	285.0	2.1
			O—$\underline{C}$— (u)	286.9	2.1
			M(—O—)$_2\underline{C}$=O bi	289.2	2.1
	O 1s			531.5	3.1
	Mg 2p			50.4	2.2
	Si 2p			102.7	2.3
	Cs 3d			725.5	2.3
Carbonated 10% Cs-doped chrysotile	C 1s	▼	C—$\underline{C}$—C, $\underline{C}$—H	285.0	1.6
			M—(O—)$_3\underline{C}$ (u)	286.3	1.6
			(MO—)$_2\underline{C}$=O (br)	288.0	1.6
			$\underline{C}O_3^{2-}$	290.3	1.0
	O 1s			532.0	2.4
	Mg 2p			50.6	2.5
	Si 2p			103.3	2.4
	Cs 3d			725.2	2.3
Commercial $MgCO_3$	C 1s	▼	C—$\underline{C}$—C, $\underline{C}$—H	285.0	1.5
			M—(O—)$_3\underline{C}$ (u)	286.2	1.4
			(MO—)$_2\underline{C}$=O (br)	287.7	1.4
			$\underline{C}O_3^{2-}$	290.2	1.7
	O 1s			531.9	2.2
	Mg 2p			50.4	1.7

[a] Full width at half maximum.
[b] M = Mg, Cs; **br** = bridging carbonate, **bi** = bidentate carbonate, **u** = unidentate carbonate with possible surface bicarbonate MO—$\underline{C}$(OH)=O in-between.

possible. These assignments were attempted on the basis of electron density displacements for carbon as inferred from the FTIR observed species (Evans and Whateley, 1967; Philipp and Fujimoto, 1992).

The MgO and $MgCO_3$ spectra were fitted using only two peaks. For the latter, the peak at $BE = 290.2$ eV and $FWHM = 1.7$ eV was assigned to surface carbonate species, CO_3^{2-}. The periclase higher-energy peak was relatively broad and was centered at BE slightly below that of car-

bonate. It was assigned to surface bidentate carboxylic entities.

The fit of the C 1s carbonated chrysotile sample required four peaks, whereas three were sufficient for the other chrysotile materials (Fig. 2). A prominent carbonate peak at $BE = 290.3$ eV was visible on the carbonated Cs-doped chrysotile which will be attributed to hydromagnesite; in addition to the feature at $BE = 286.3$ eV, possibly related to M—(O—)$_3$**C** (u) species. This unidentate species is also
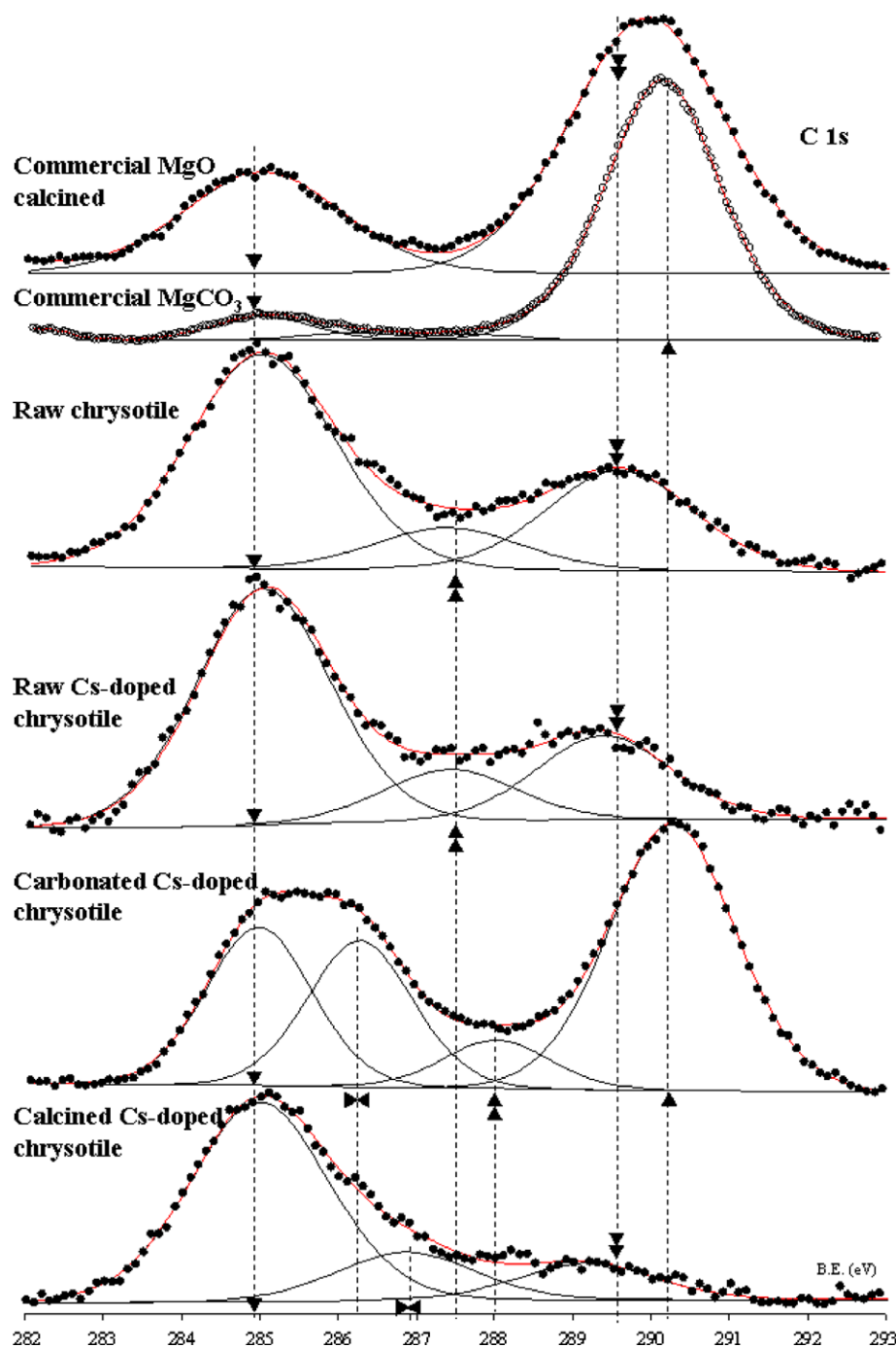
Fig. 2. High-resolution XP C 1s core level spectra along with fitted features as shown in Table 2 for unreacted chrysotile and Cs-doped chrysotile, moist-carbonated Cs-doped chrysotile and calcined post-carbonated Cs-doped chrysotile, commercial MgO and $MgCO_3$.
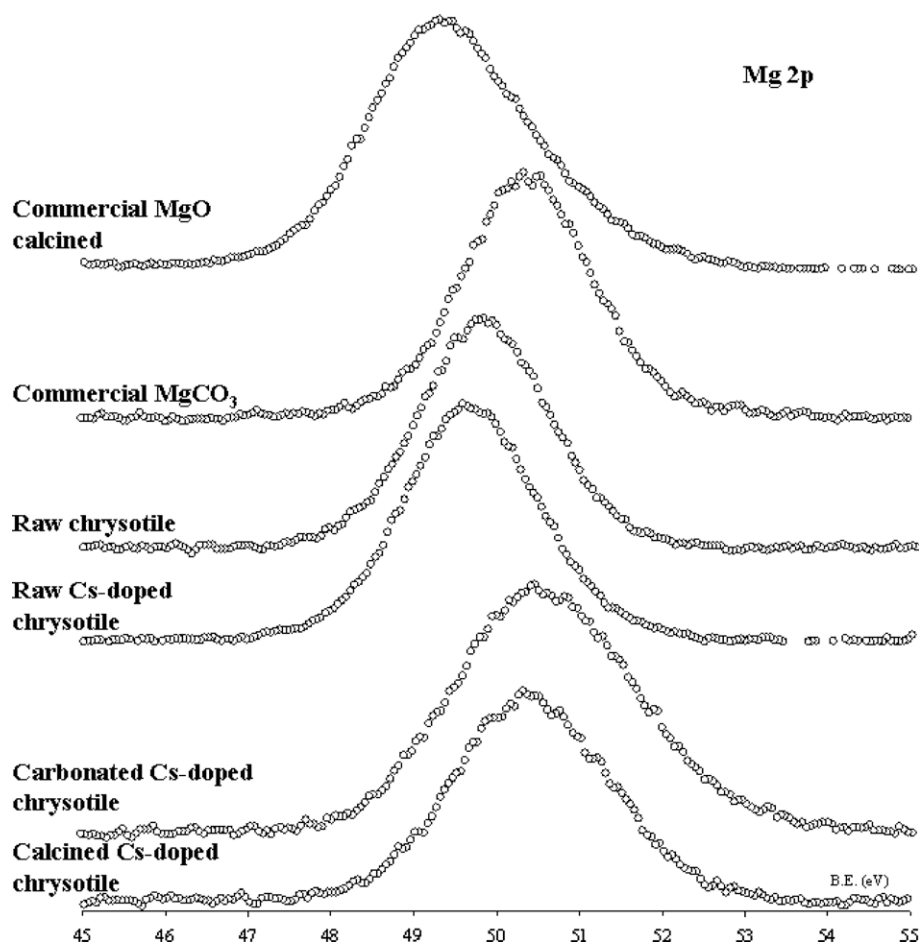
Fig. 3. High-resolution XP Mg 2p core level spectra for unreacted chrysotile and Cs-doped chrysotile, moist-carbonated Cs-doped chrysotile and calcined post-carbonated Cs-doped chrysotile, commercial MgO and MgCO$_3$.

visible near 286.9 eV after calcination of post-carbonated chrysotile and near 286.2 eV for the commercial magnesium carbonate.

The surface alterations for silica and dicesium monoxide and how they compare with respect to C 1s modifications in unreacted, carbonated (at 375 °C) and then calcined (500 °C) chrysotile are shown, respectively, in Figs. EA-1-2 and EA-1-3. Silica was used in provision of potential silicate formation at high temperatures, e.g., highly disordered tridymite-like phases (Candella et al., 2007). Similarly, Cs$_2$O can also fixate some of the captured CO$_2$. Fig. EA-1-2 indicates that silica carbonation at 375 °C barely changed the carbonate signature at BE = 290.2 eV as identified in the unreacted silica. However, carbonation of cesium oxide at 375 °C is beyond doubt with a BE near 286.6 eV. It is highly probable that this cesium carbonate feature merges with the carbonate shift associated with hydromagnesite species to be discussed later.

Fig. 3 illustrates the Mg 2p high resolution XP spectra for the series exemplified in Fig. 2. Calcined commercial periclase gave the lowest Mg 2p BE ≈ 49.2 eV and commercial magnesite (BE ≈ 50.4 eV) was surpassed only slightly by the carbonated Cs-doped chrysotile (BE ≈ 50.6 eV). Mg 2p core electrons in the unreacted bare and Cs-doped

chrysotile exhibit slightly larger BE than in the case of periclase with a tendency for Mg 2p binding energy to shift to higher values after carbonation. This shift in BE of Mg 2p core electrons upon carbonation is unlike the observations reported by Schulze et al. (2004) on the hydrothermal carbonation of lizardite in a high-pressure high-temperature slurry reactor. Mg 2p core electrons shifted to higher BEs not because of carbonation of lizardite but due to preliminary thermal treatment of the material. Thomassin et al. (1977) in their XPS study of Québec chrysotile leaching in oxalic acid too did not report significant changes in the chemistry of its elements.

Similarly, Cs 3d$_{5/2}$ XP spectra are detailed in Fig. 4. Unlike the diminishing shifts reported in Reddy and Smirniotis (2004) regarding Cs 3d$_{5/2}$ BE from calcined to carbonated Cs-doped CaO supports, Cs 3d$_{5/2}$ core electrons' spectra in our study exhibited an opposite trend, though coherent with Si 2p and Mg 2p shifts as previously shown. Cs 3d$_{5/2}$ BE hardly increased by 0.2 eV from unreacted to moist carbonated Cs-doped chrysotile (Table 2). However, upon calcination the initial oxidation state of Cs was not restored and the binding energy for Cs 3d$_{5/2}$ kept climbing by an extra 0.3 eV (Table 2). The same qualitative shift, albeit more substantial, was also observed in the case of commercial ce-

Cs 3d

Commercial Cs₂O
calcined

Commercial Cs₂O
carbonated

Commercial Cs₂O

Raw Cs-doped
chrysotile

Carbonated Cs-doped
chrysotile

Calcined Cs-doped
chrysotile

B.E. (eV)

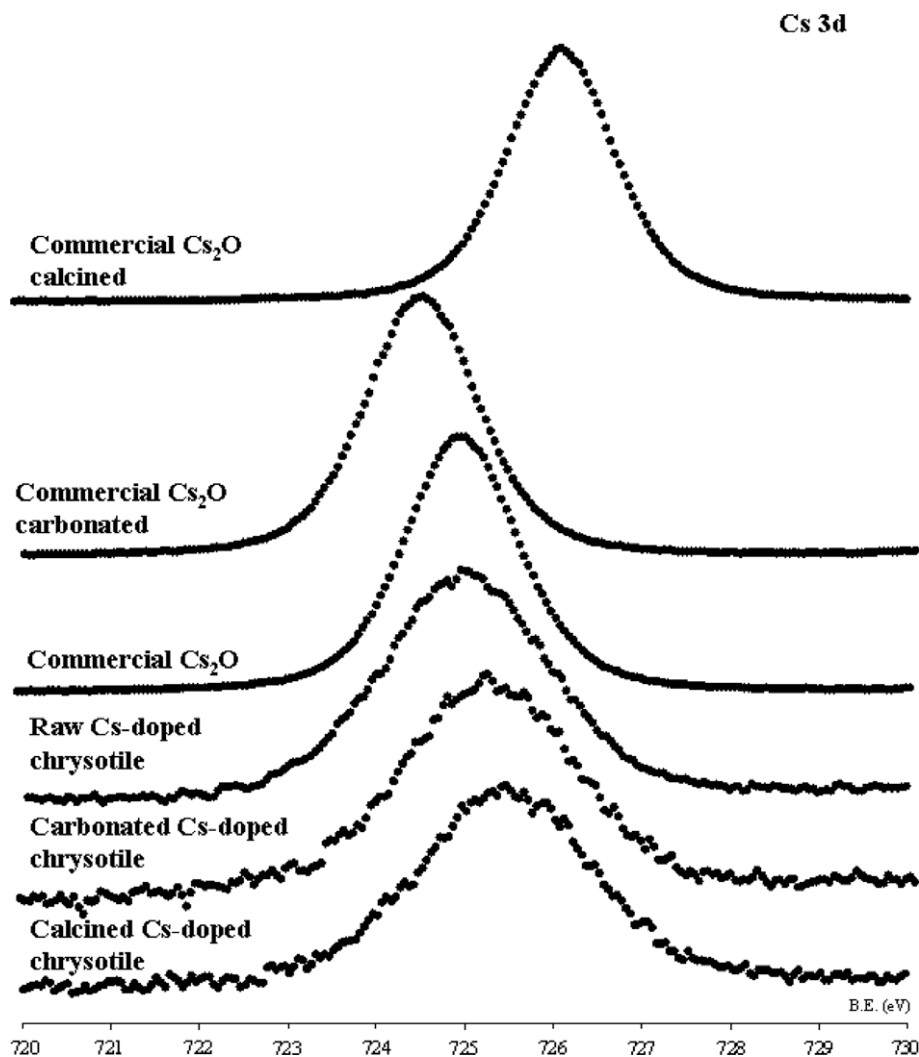720   721   722   723   724   725   726   727   728   729   730

Fig. 4. High-resolution XP Cs 3d$_{5/2}$ core level spectra for Cs-doped chrysotile, moist-carbonated Cs-doped chrysotile and calcined post-carbonated Cs-doped chrysotile, commercial cesium oxide, carbonated and then calcined.

sium oxide calcined after carbonation (Fig. 4). According to the NIST database, a BE of 725.1 eV would correspond to Cs 3d$_{5/2}$ in Cs₂O in agreement with our findings. We refrained, however, from making assignments to cesium carbonates based on the small shifts revealed from Fig. 4.

4.2. Ex-situ characterization

Three XRPD series corresponding to chrysotile evolved in various TGA conditions have been obtained. Fig. 5a illustrates the X-ray powder diffraction patterns of raw chrysotile and chrysotile calcined from 300 to 1200 °C. Those for dry carbonation of chrysotile at the corresponding temperatures are displayed in Fig. 5b. The XRPD results in Fig. 5c correspond to bare chrysotile **[i]** and Cs-doped chrysotile **[iii]** carbonated under controlled moisture at 375 °C and followed by calcination at 500 °C, curves **[ii]** and **[iv]**, respectively. With reference to the raw material, the loss in BET surface area and the increase in average pore diameter were, respectively, by a factor 3.3 and 12 with

increasing temperatures (Table 3). Some scanning electron micrographs show the change in chrysotile morphology (Fig. EA-1-6 in Electronic annex).

The transformations hinted from Fig. 5a are more or less in agreement with several studies on XRPD of calcined chrysotile in inert gas H₂O-autogenous environments. The main diffraction peaks associated with interlamellar spacing along planes (0 0 2): $2\theta = 12.0° \equiv 7.36$ nm; (0 0 4): $2\theta = 24.3° \equiv 3.66$ nm; and ($\bar{1}$ 3 2): $2\theta = 36.6° \equiv 2.46$ nm reflect chrysotile crystalline pattern. Breakdown of chrysotile structure is underway from 500 °C and onwards as sensed from the dramatic collapse of these main peaks. Except for a remnant low-scattering-angle poorly-ordered feature, complete obliteration of organized crystalline structure was reached at 600 °C where the so-called dehydroxylated amorphous *meta*-chrysotile, Mg₃Si₂O₇, will have supplanted chrysotile (Falini et al., 2004; Candella et al., 2007). Incipience of forsterite, interspersed in the amorphous matrix, was palpable from 600 °C. A firm forsterite structure predominates at 900 °C, albeit slightly muted near
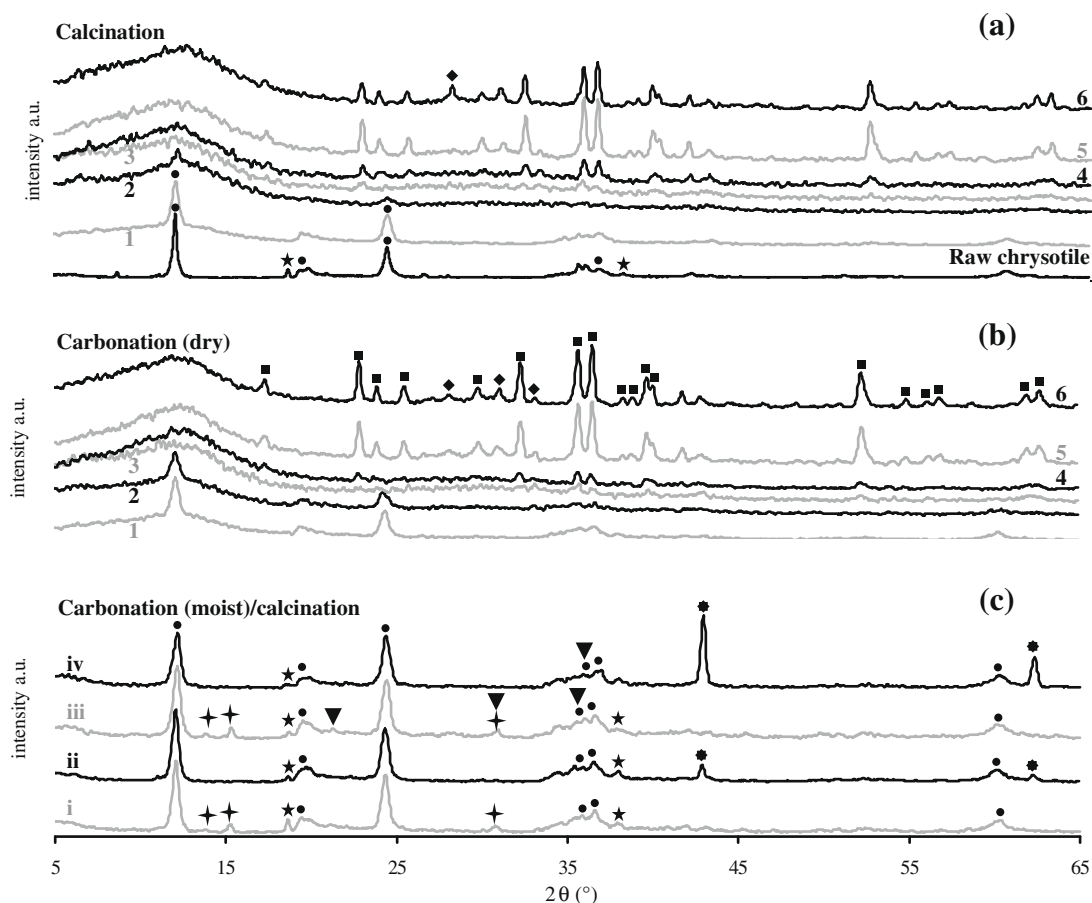
Fig. 5. X-ray powder diffraction patterns of (a) raw chrysotile and chrysotile calcined at $T =$ [1] 300 °C; [2] 500 °C; [3] 600 °C; [4] 700 °C; [5] 900 °C; [6] 1200 °C. (b) Dry carbonation at $T =$ [1] 300 °C; [2] 500 °C; [3] 600 °C; [4] 700 °C; [5] 900 °C; [6] 1200 °C. (c) Hydrothermal carbonation ($CO_2 + 6.7$ mol % H_2O/He) followed by calcination: carbonation of chrysotile [i] at 375 °C and subsequent calcination [ii] at 500 °C, carbonation of Cs-loaded chrysotile [iii] at 375 °C & subsequent calcination [iv] at 500 °C. (●) chrysotile, (★) brucite, (■) forsterite, (♦) enstatite, (✱) periclase, (✚) hydromagnesite, (▼) cesium oxide.

Table 3
BET specific surface areas and BJH average pore diameters for raw and alkali-oxide-doped chrysotile under calcination (150 NmL/min He), dry (100 NmL/min CO_2 + 50 NmL/min He) and moist (90 NmL/min CO_2 + 10 NmL/min H_2O + 50 NmL/min He) carbonation at different temperatures.

Sample	Surface area (m²/g)	d_p (nm)
Raw chrysotile	14.4	5.5
10% Li-doped chrysotile	4.8	10.1
10% Na-doped chrysotile	6.5	7.9
10% K-doped chrysotile	7.1	5.5
10% Cs-doped chrysotile	8.2	3.7
Calcined $T = 300$ °C	13.0	8.7
Calcined $T = 500$ °C	10.0	8.6
Calcined $T = 600$ °C	10.7	9.3
Calcined $T = 700$ °C	8.4	11.8
Calcined $T = 900$ °C	6.3	47.2
Calcined $T = 1200$ °C	4.4	65.9
Dry carbonation $T = 300$ °C	8.6	25.1
Dry carbonation $T = 500$ °C	7.0	73.4
Dry carbonation $T = 700$ °C	4.7	84.7
Dry carbonation $T = 900$ °C	3.4	85.5
Dry carbonation $T = 1200$ °C	0.8	96.9
Moist carbonation $T = 375$ °C	9.3	6.4
Moist carbonation 10% Cs-doped chrysotile $T = 375$ °C	6.2	5.3

900 °C with the emergence of enstatite whose crystal growth is already perceivable between 700 and 900 °C. Native brucite, coexisting with raw chrysotile, is distinguishable (Fig. 5a). Its dehydroxylation is thermodynamically favorable after about 250 °C with resulting periclase overrun by the emerging amorphous *meta*-chrysotile.

It is instructive to observe that already by 300 °C, a relatively broad bump protrudes near $2\theta = 12.0°$ inflating the baseline around the (0 0 2) peak. This bump reveals emergence of a pseudo-amorphous poorly-ordered entity, well before amorphous *meta*-chrysotile is known to have entirely taken over chrysotile from 600 °C. This poorly-ordered component gains in height with increasing temperatures and then presumably evolves into a *meta*-chrysotile phase coexisting along with forsterite and enstatite at higher temperatures. It is speculated that the diffraction planes (0 0 2) and (0 0 4), drawn in Fig. 1c, are very sensitive to lattice distortions induced after 300 °C by a gradual inter-bilayer seepage of structural water within the **T–O···T–O** intra-nanofibrilar space. Water seepage starts likely as a mono-dehydroxylation process involving the outer OH groups overhanging on top of the *core* Mg in $Mg_3Si_2O_5(OH)_4$ (Fig. 1c) to yield an inter-grown metastable dioctahedral monodehydroxylated chrysotile intermediate, with stoichiometry $Mg_2Si_2O_6 \cdot H_2O$. This intermediate likely goes along with the inchoate periclase-type magnesium still confined within. This $Mg_2Si_2O_6 \cdot H_2O$ entity is thought to contribute to the large bump centered at $2\theta = 12.0°$ below 600 °C. In addition, since intra-layer strain is minimal for a radius of curvature of 8.8 nm (Evans, 2004), it could imply that most of the nanofibril material grown in the thickness contained in that part with diameters greater than 2×8.8 nm would be more vulnerable to an early monodehydroxylation thus causing the inception of the low-scattering angle XRPD feature (Fig. 5a). Progressively, this intermediate would acquire an amorphous character, as temperatures increased (Fig. 5a), in line with its gradual conversion into *meta*-chrysotile.

Structural gradation from chrysotile coexisting with its pseudo-amorphous off-spring, to *meta*-chrysotile, and ultimately to forsterite/enstatite coexisting phases shares several commonalities with recent low-pressure decomposition studies of chrysotile by Candella et al. (2007) who showed that phase-demarcation temperatures depend to a large extent on the time–temperature exposure protocol. Lizardite, a chrysotile polymorph, shares common qualitative features as regards the formation of α- and poorly-ordered *meta*-serpentines with rising temperature as discussed by McKelvy et al. (2004).

Dry carbonation, as shown in Fig. 5b, remained qualitatively shiftless vis-à-vis the features highlighted during the calcination isotherms (Fig. 5a). However, the reductions in BET specific surface areas, as mirrored by the increased pore diameters, were much more dramatic in the presence of CO_2 than under neutral H_2O-depleted atmosphere (Table 3). No crystalline magnesite was detected from ex-situ XRPD.

Moist carbonation followed by dry calcination reveals new and different XRPD features (Fig. 5c). Crystalline magnesite is not detectable. Formation of crystalline hydro-

magnesite ($2\theta \approx 13.8°$, 14.3°, 30.7°) and brucite ($2\theta \approx 18.7°$, 38.0°) is unambiguous for both unpromoted **[i]** and Cs-doped chrysotile **[iii]**. Previous field observations by Huot et al. (2003) have shown that spontaneous carbonation under weathering conditions forms hydromagnesite within chrysotile residues in southern Québec. This tends to support our laboratory observation regarding thermodynamically favorable formation paths of hydromagnesite. Some crystalline features due to cesium oxide can also be unveiled on the post-carbonated Cs-doped chrysotile sample **[iii]**. Such features, despite a 3% Cs/Mg atom ratio, are still visible from XRPD, and from XPS as well in accordance with Figs. 2 and EA-1-3. Hydromagnesite was no longer discernable on the samples after these were subsequently calcined at 500 °C (curves **[ii]** and **[iv]**). However, small amounts of leftover crystalline brucite remained detectable. Furthermore, peaks attributed to crystalline periclase appear at $2\theta \approx 43.0°$, 62.2°. The pseudo-amorphous bump around the chrysotile main diffraction peak associated with (0 0 2) plane is no longer observed on all post-carbonated and post-calcined samples (Fig. 5c).

4.3. Chrysotile structure and rationale for its carbonation reactivity

Chrysotile with an ideal trioctahedral **T–O** unit in the unit cell belongs to space group *Cc* with lattice constants $a = 0.534$ nm, $b = 0.9241$ nm, and $c = 1.4689$ nm (Falini et al., 2004). These lattice constants combined with the Mg, Si, and O atomic coordinates allow calculating the $(H)O \leftrightarrow O(H)$ inter-atomic distances of the scalene triangle formed by the three outermost hydroxyl groups (Fig. 1) as well as the diameter of the corresponding inscribed circle (whereby H_2O and CO_2 would crisscross along *c* direction). Our calculations give 0.3035(6), 0.3190(6), and 0.3263(8) nm for the triangle side lengths and 0.1821(5) nm for the inscribed circle diameter. In addition, the inter-atomic distances between the three Mg in each $Mg_3Si_2O_5(OH)_4$ nanocrystal are 0.3008(3), 0.3027(2), and 0.3189(3) nm. The shortest and longest distances between two vicinal Mg in the unit cell of crystalline brucite, are 0.315 and 0.477 nm, respectively (Lin et al., 2008). These inter-atomic distances combined with the CO_2 and H_2O van der Waals molecular diameters of, respectively, 0.47 nm (Goel, 2006) and 0.282 nm (Chieh, 2005) allow us to assess the H_2O and CO_2 cross-over during (de)hydroxylation/carbonation. Unlike chrysotile, brucite offers openings more compatible with the CO_2 van der Waals sphere diameter. Hence, chrysotile reactivity is anticipated to be severely impaired by its intrinsic geometrical structure.

Proton transfer mechanisms are well understood in the case of brucite dehydroxylation and could serve as a basis for a mechanistic interpretation of chrysotile dehydroxylation and carbonation in dry (Kalinichenko and Litovchenko, 2000; McKelvy et al., 2001) and in moist (Nahdi et al., 2009) environments. Thermodynamic considerations and simple calculations suggest incipient structural water would be driven off the chrysotile **T–O** unit through proton-transfer (and vacancy pop-up) monodehydroxylation of its outermost hydroxyl groups in the first place (step
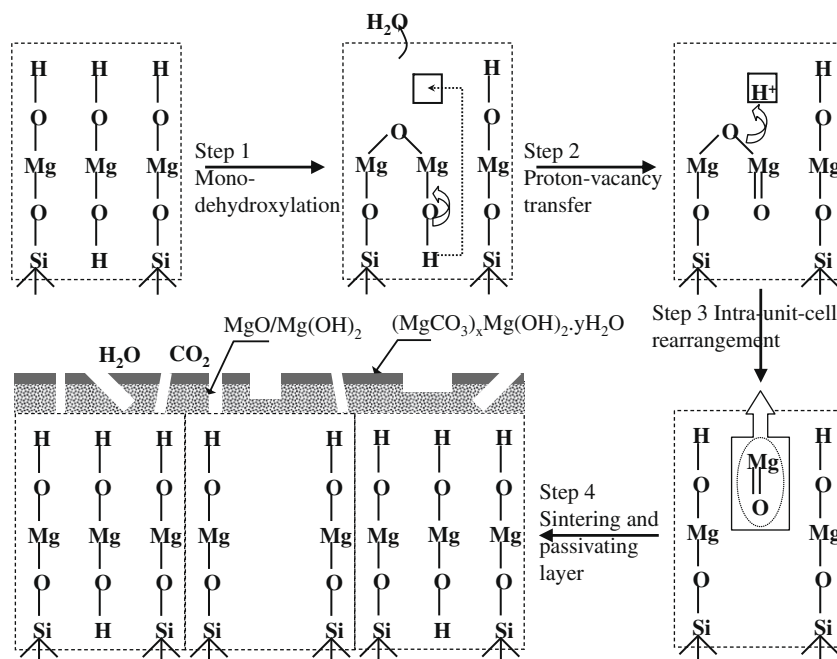
Fig. 6. Mechanistic speculation on chrysotile carbonation through a monodehydroxylation route of its core (brucitic) Mg: step (1) monodehydroxylation via lateral (HO)Mg//core (HO)Mg proton transfer and vacancy pop-up, step (2) core-Mg proton transfer to vacancy, step (3) intra-unit-cell rearrangement with nucleation of periclase, step (4) formation of hydromagnesite passivation layer, nearby or atop of brucite, impeding further dehydroxylation and carbonation.

(1), Fig. 6). This occurs at the expense of the innermost core-Mg-bonded OH whose participation in dehydroxylation is less probable. Instead, it would be much easier for a proton from this innermost OH to subsequently migrate upwards to fill up the vacant site left past (step (2)) dehydroxylation. In this intermediate state, intra-unit-cell rearrangement and trans-lamellar MgO nucleation (step (3), Fig. 6) would presumably give rise to the aforementioned metastable dioctahedral monodehydroxylated chrysotile intermediate, $Mg_2Si_2O_6 \cdot H_2O$, as well as reactive MgO to be carbonated. This mechanism hence views the core Mg (with brucitic inheritance) as more reactive than the two Si-attached *lateral* Mg in a T–O unit.

Diffusion retardation and accumulation of H_2O molecules nearby the lattice structures, during sample cooling following moist carbonations, could be responsible for the formation of crystalline brucite (Fig. 5c). However, crystalline phases of Mg carbonates, brucite or periclase were not detected following dry carbonation (Fig. 5b). Conversely, brucite and hydromagnesite crystalline phases have been identified as two plausible chrysotile moist carbonation end-products (Fig. 5c). Water vapor is believed to play a role as a sintering facilitator (Béarat et al., 2002) of nucleated trans-lamellar MgO and would explain the inception of crystalline MgO in post-(moist)carbonation calcination conditions (Fig. 5c). Exogenous H_2O is also believed to stabilize, during carbonation, the carbonates in their hydrous forms such as hydromagnesite and, though not monitored in-situ, presumably also as artinite or nesquehonite (as suggested on thermodynamic grounds by Königsberger et al., 1999). That the formation of an uppermost hydromagnesite passivating layer could be the cause of the low chrysotile

reactivity, in accordance with the TGA studies, seems kinetically plausible (step (4), Fig. 6) and not conflicting with thermodynamics as discussed later.

Further, in our proposed mechanistic abstraction, there is no requirement for pure silicate formation that might require much higher reaction temperatures ($T > 600 °C$) to form highly disordered tridymite-like phases as observed by Candella et al. (2007).

4.4. TGA–MS reaction studies

Water adsorption on unreacted, raw and promoted, chrysotile fibers was found to contribute 2.2–3.9 mg/g (Fig. 7a). For P_{H_2O} partial pressures equal to 0.067 atm in the TGA, the $P_{H_2O}/P_{sat}(T)$ varied between 3.2×10^{-4} and 1.53×10^{-2} for temperatures ranging between 150 and 375 °C, where $P_{sat}(T)$ is the water vapor saturated pressure at temperature T. Under those conditions, the Kelvin equation predicts water storage by capillary condensation is no longer conceivable (Kelvin meniscus curvature diameters $\ll 1$ nm). On a per 100 chrysotile molecules basis, water fixation dropped from ca. 7 water molecules at 150 °C to ca. 4 at 475 °C. Based on data from Jolicoeur et al. (1981), water uptake (adsorption) at ambient temperature on Québec chrysotile fibers gave nearly 70 mg/g with an estimated pore diameter equal to 20 nm for condensation to take place. This gives one water molecule for each chrysotile molecule for water sorption at ambient temperature. The decrease of water sorption on chrysotile as temperature increases as well as the order of magnitude of mass retention (Fig. 7a) seems more in line with a multilayer adsorption of water on *hydrophilic* surfaces as measured by Gruszkiewicz
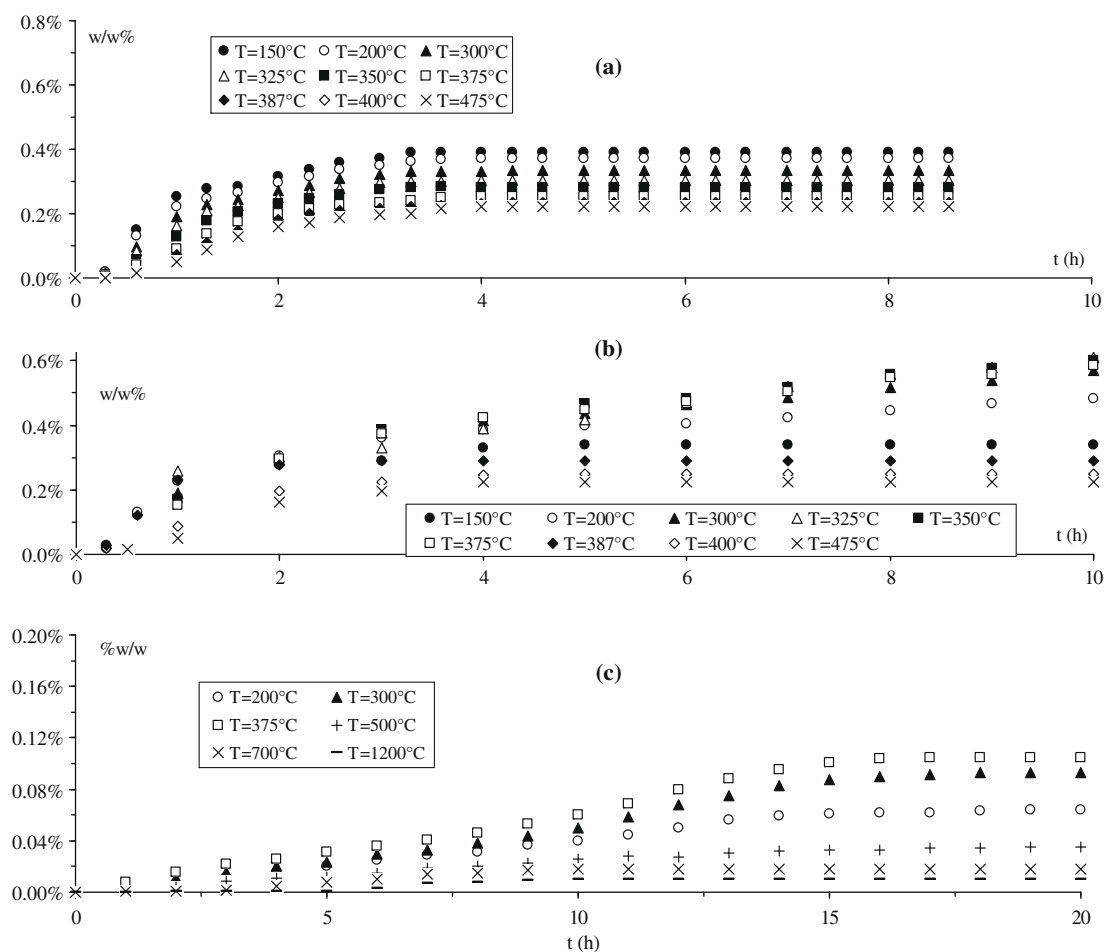
Fig. 7. Time evolution on bare chrysotile at different temperatures of (a) water uptake (no CO_2 present), (b) net $CO_2 + H_2O$ uptake during moist carbonation: CO_2 (90 NmL/min)/H_2O (10 NmL/min)/He (50 NmL/min), (c) net $CO_2 + H_2O$ during dry carbonation: CO_2 (100 NmL/min)/He (50 NmL/min). $P_{total} = 0.1$ MPa.

et al. (2001) on geothermal reservoir rocks using an isopiestic technique.

The van der Waals molecular diameter for water is close to that of N_2, i.e., 0.29 nm (Li et al., 2007). Thus, as a first approximation, the BET surface areas corresponding to N_2 or to H_2O sorption could be viewed as comparable. Considering the molecular areas for adsorption as half the shell area of the van der Waals sphere, the water BET adsorption areas were calculated from the limiting water uptake after equilibrium was reached (Fig. 7a). The resulting specific surface areas for water decreased monotonically from 16.3 m^2/g (at 150 °C) to 9.3 m^2/g (at 475 °C). These areas amounted, respectively, to 114% and 65% of the measured N_2 BET surface area for raw chrysotile. This could suggest that H_2O was physisorbed as fragmented monolayer islands, or perhaps, as one single monolayer. However, these figures appear to be rather large considering the tested temperatures. It is not unlikely that a portion of H_2O would have been adsorbed by some irreversible chemisorption reactions, e.g., with the coexisting sample impurities.

Fig. 7b and c illustrates the net $CO_2 + H_2O$ uptake in isothermal moist and dry carbonation of unpromoted chrysotile as a function of time and temperature. An induc-

tion phase was always required before the reaction rate increased dramatically. At 375 °C, chrysotile reactivity was the highest after about 5 h exposures showing less than 0.5% conversion (for carbonated Mg) in moist carbonation and less then 0.1% in dry carbonation (Fig. 7b and c). In comparison, brucite at 375 °C was reported to be relatively more reactive showing about 6.5% conversion after 12 h at 1 atm CO_2 in an H_2O-depleted environment (Butt et al., 1996). One may argue that these numbers can be shadowed by direct carbonation of the native brucite which amounts, according to XRF analysis, to 1.2% Mg (molar basis) in the raw chrysotile. Notwithstanding, without setting aside native brucite reactivity, this contention would be indefensible considering the prominent appearance of crystalline MgO after calcing at 500 °C the post-(moist)carbonated chrysotile at 300 °C (Fig. 5c), not to mention the absence of crystalline MgO in the dry calcination and dry carbonation tests of chrysotile at the same temperatures (Fig. 5a and b).

The small mass changes recorded by TGA reveal tepid kinetic lability of chrysotile to carbonation. This mass change corresponds to simultaneous carbonation and dehydroxylation in dry carbonation (Fig. 7c), and likely carbonation accompanied by water fixation in moist carbonation
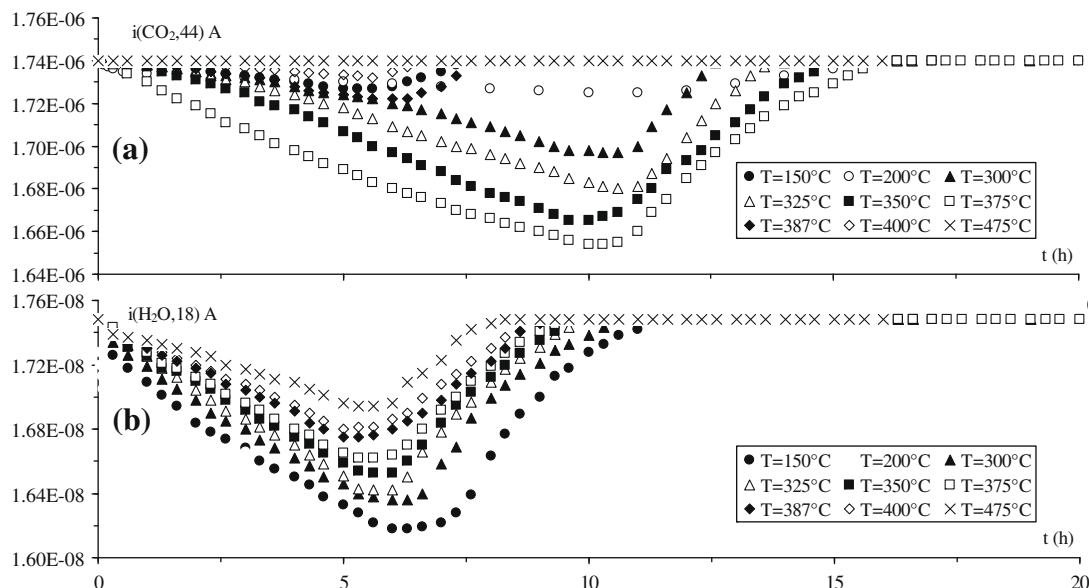
Fig. 8. Time evolution during moist carbonation of bare chrysotile at different temperatures of (a) positive ion current $m/z = 44$ (CO_2), (b) positive ion current $m/z = 18$ (H_2O): CO_2 (90 NmL/min)/H_2O (10 NmL/min)/He (50 NmL/min). $P_{total} = 0.1$ MPa.

(Fig. 7b) as confirmed by dipping MS signals of Fig. 8a and b. Fixation of exogenous water, as highlighted in Fig. 8b, has multiple roles: (i) incorporation and stabilization as surface hydrous magnesium carbonates: $(MgCO_3)_x Mg(OH)_2 \cdot yH_2O$ (Fig. 5c); (ii) parasitic chemisorption on non-chrysotile sites (Fig. 7a); (iii) amorphisation accelerator of the chrysotile intermediate, $Mg_2Si_2O_6 \cdot H_2O$ to free the associated embedded periclase-type Mg, promoting carbonation; (iv) sintering facilitator (Béarat et al., 2002) of nucleated trans-lamellar MgO which would explain inception of crystalline MgO in post-(moist)carbonation calcination conditions (Fig. 5c). Mobility across the chrysotile network of H_2O molecules in these processes is necessary and compatible with the lattice sizes in chrysotile. This seems supported by relaxation time measurements using high-resolution quasi-elastic neutron scattering by Mamontov et al. (2005) who showed that diffusion of H_2O in chrysotile revealed insignificant anisotropy with the scattering vector parallel and perpendicular to the fiber axes.

The MS signals of Fig. 8a and b reveal different water and CO_2 dynamics as temperatures rises. The dip in H_2O^+ current showcases a monotonic decrease with increasing temperature. This is attributed to decreasing water uptake as revealed in Fig. 7a for CO_2-deprived moist streams at increasing temperatures. The CO_2^+ current exhibited, on the contrary, a non-monotonic behavior with the lowest value attained at 375 °C, i.e., temperature for highest carbonation activity (see below for further discussion), and no CO_2 consumption at all at 475 °C (Fig. 10). Also, carbonation of chrysotile continues long after water interactions with the support have ceased. This behavior seems logical with the development of a passivating hydromagnesite layer which forbids further access to water (Fig. 6) as also suggested by the much slower water dynamics, 10 h versus 4 h, either in the presence (Fig. 8b) or in absence, of CO_2 (Fig. 7a)

4.4.1. Inferring the amount of CO_2 fixation on chrysotile and topochemical considerations

The TGA signal, $W_{CO_2+H_2O}$, is global and comprises the combined CO_2 (gain) and H_2O (loss or gain) during carbonation. At this point, one can only infer the amount of CO_2 contributing to chrysotile carbonation. Fig. 9 allows one to sort the mass gain contributed by CO_2 during moist carbonation in the case of raw chrysotile (Fig. 9a) and of Cs-promoted chrysotile (Fig. 9b). Fig. 9c shows the evolution of the MS signals of H_2O^+ and CO_2^+ ion currents. The reactivity of chrysotile and Cs-doped chrysotile in single-step moist carbonation at 375 °C is compared with two-step carbonation consisting of CO_2-free steam-treatment for ca. 5.5 h immediately relayed by H_2O-deprived carbonation at the same temperature of 375 °C. The ultimate mass gain was not different whichever single- or two-step carbonation was implemented. Though not captured because the 2 h time increment was too large in the one-step carbonation in Fig. 10, the one-step carbonation uptakes systematically exhibited a low-slope induction phase (lasting ca. 30 min; Figs. 8b, 12a, and 14). However, with steam pre-treatment, no induction phase was visible after the (dry) carbonations were resumed (after arrow, Fig. 9a and b). This indicates that the initial reaction rate of carbonation is accelerated by availability of water on the chrysotile surface and without affecting the plateau values of the net uptakes for the single- and the two-step moist carbonations. It is possible that part of the amorphised chrysotile, whose formation is accelerated by H_2O, makes its associated periclase-like Mg more accessible (Fig. 6) explaining steeper initial carbonation rates (Fig. 9a and b).

Interestingly, the MS water current signals ($<10^{-4}$ μA) following resumption of dry carbonation (marked by the vertical arrow in Fig. 9) dropped by more than two-order of magnitudes below the water dip registered near
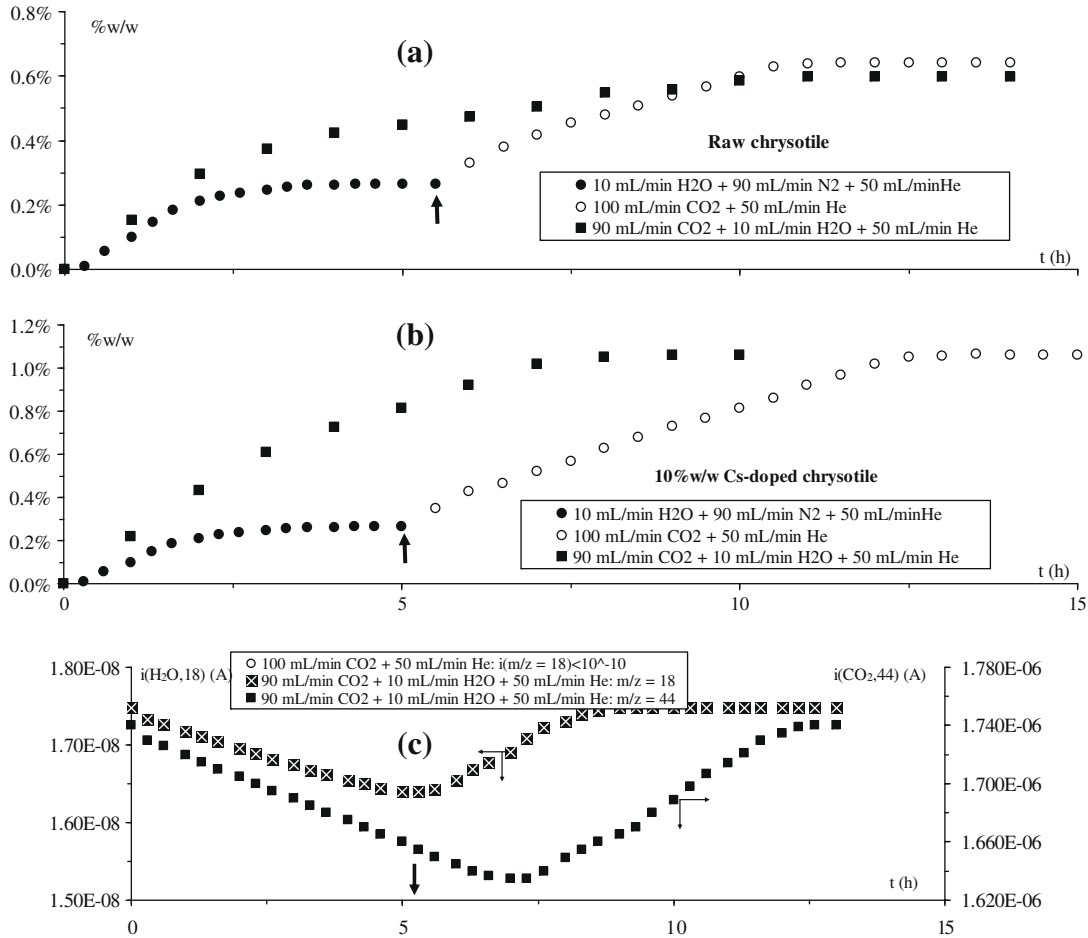
Fig. 9. Comparison of reactivities at 375 °C of single-step moist carbonation with two-step carbonation consisting of CO_2-deprived steam-treatment for 5.5 h (H_2O (10 NmL)/N_2 (90 NmL/min)/He (50 NmL/min)) relayed by H_2O-deprived dry carbonation treatment (CO_2 (100 NmL/min) + He (50 NmL/min)). Net mass gain $W_{CO_2+H_2O}$ in w/w% for (a) raw chrysotile, (b) Cs-doped chrysotile, (c) positive ion currents at $m/z = 44$ and $m/z = 18$ (H_2O) in single-step moist carbonation. $P_{total} = 0.1$ MPa.

1.65×10^{-2} μA in the single-step moist carbonation. This suggests that CO_2 impinging on chrysotile in the two-step carbonation acts as an impermeable curtain retaining the fixated water. Hence, CO_2 should represent the exclusive source for mass change in this subsequent step for both bare and unpromoted materials (Fig. 9a and b). As a consequence, a means to account for CO_2 separate contribution out of the total TGA signal could be possible at least on the plateau portion.

By combining TGA, BET surface area measurement and structural data, it is possible to estimate how many surface magnesium atoms are being carbonated. It is reasonable to assume that the effective interaction area of every *core* Mg atom of the **O** sheet be given by the area, A_Δ, formed by the scalene triangle delineated by the three outermost hydroxyl groups.

Hence, A_Δ ($= 4.3215$ Å^2) and BET surface area SSA_{BET} ($= 14.4$ m^2/g) give access to an estimate of the mole concentration of *surface* core Mg per unit sample mass, {Mg}:

$$\{Mg_{core}\} = \frac{SSA_{BET}}{A_\Delta \aleph} \quad \text{in mol/g} \quad (1)$$

Similarly, according to XRF analysis (Table 1), the total number of moles of core Mg per unit sample mass located both in chrysotile bulk and surface (and neglecting native brucite Mg) is:

$$[Mg_{core}] = \frac{0.902}{M_{chrysotile}} \quad \text{in mol/g} \quad (2)$$

The moles of CO_2 fixated per unit mol of core Mg, respectively, areal and total, can be cast as follows:

$$\langle CO_2 \mid Mg \rangle = \frac{W_{CO_2+H_2O} - W_{H_2O}}{\{Mg_{core}\}M_{CO_2}} \quad \text{in mol } CO_2 \text{ per mol}$$
$$\text{of surface core Mg} \quad (3)$$

$$[CO_2 | Mg] = \frac{W_{CO_2+H_2O} - W_{H_2O}}{[Mg_{core}] M_{CO_2}} \quad \text{in mol } CO_2 \text{ per mol}$$
$$\text{of (surface + bulk) core Mg} \quad (4)$$

where $\aleph = 6.0221 \times 10^{23}$, $M_{CO2} = 44$ g/mol, and $M_{chrysotile} = 280.868$ g/mol.

The TGA data from Fig. 7a and b, following the reasoning from Fig. 9, have been converted using Eqs. (3) and (4) (Fig. 10a and b), as CO_2 fixated per unit *areal* core Mg and
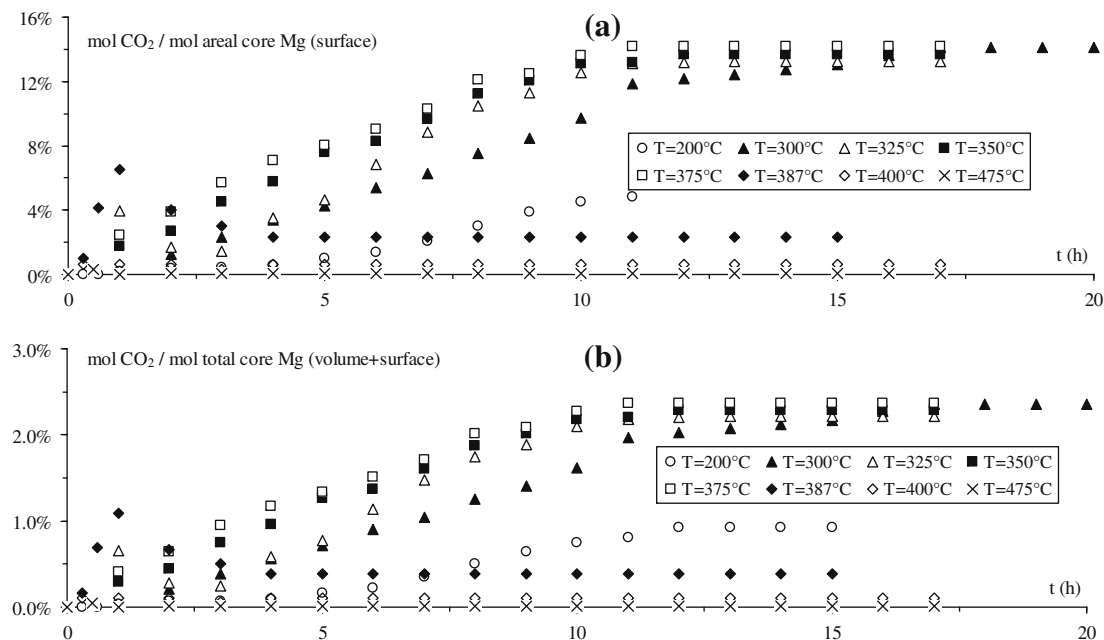
Fig. 10. Time evolution on bare chrysotile at different temperatures of (a) CO_2 mole uptake per mole of initial areal core Mg, CO_2 mole uptake per mole of total initial core Mg (volume + surface): measurement conditions similar to Fig. 8b.

per unit *total* core Mg, respectively. Hardly 15% of surface core Mg atoms, based on the fresh accessible N_2 BET area, have reacted with CO_2 which also translates into 2.5% of the total core Mg in chrysotile being utilized. These numbers mean that chrysotile amorphisation, as supported from previous XRPD and BET measurements on the post-reacted samples, was insufficient to make all the reactive MgO, buried underneath, accessible for carbonation. Hence, the important rise in average pore diameters inferred from BET measurements (Table 3) on the reacted samples make sense only if the newly-forming magnesium carbonate hydrates quickly clog the nanofibril's outer surface thus barring access to the deeper layers and limiting the reacted surface volume. Fig. 9 results could also be interpreted as H_2O circulation being less hindered than that of CO_2-bearing species, which explains the faster initial reaction rates in the two-step process without the ultimate net uptake being affected in the case of either the single- or two-step carbonation reactions. The remarkable buildup of crystalline MgO (XRPD patterns of Fig. 5c) is post-facto evidence of potentially available reactive MgO not reachable by CO_2. Recall that such a crystalline MgO phase did not occur during either dry carbonation or dry calcination (Fig. 5a and b).

Let us now estimate the contribution to carbonation from Mg atoms that would stem from the brucite impurities. Brucite contamination contributes for 0.67 wt% of the chrysotile sample, or, equivalently 12 Mg atoms out of 10^3 belong to brucite. Recall that 375 °C is the temperature showing the highest carbonation for chrysotile (Figs. 7b and c, 10a and b). According to Butt et al. (1996), 12.1 Mg atoms out of 100 Mg atoms (conversion = 12.1%) were carbonated after 12 h carbonation test of pure brucite

under pure CO_2 atmosphere (1 atm) at 375 °C (computed from their Fig. 7, P. 1896). It is plausible to assume that this conversion is a conservative *upper limit* applicable to the brucite impurities contained in our chrysotile sample. Hence, out of 15 *carbonated* Mg atoms (Fig. 10a and b), a maximum of $3 \times 10^2/2.5 \times 12/10^3 \times 12.1/10^2 \times 15 = 2.6$ Mg atoms would be contributed from brucite. This indicates that *at least* 82.4% of the carbonatable magnesium was contributed from chrysotile. Thus, the carbonation contribution from brucite impurities could be viewed as minor and that magnesium chrysotile in our tested conditions is reactive enough to explain the changes observed from Figs. 7b and c, 10a and b.

4.4.2. Effect of CO_2 and H_2O composition on chrysotile carbonation

The effect of CO_2 composition during moist carbonation of raw chrysotile at 375 °C is shown in Fig. 11a in terms of overall mass gain $W_{CO_2+H_2O}$ (w/w%) and constant H_2O feed mole fraction. The corresponding positive ion currents at $m/z = 44$ and $m/z = 18$ are shown in Fig. 11b and c. Increasing CO_2 mole fraction in the gas stream enhanced slightly the carbonation rate without affecting the carbonation plateau. Water uptake at the same mole fraction in absence of CO_2 and identical temperature is shown in Fig. 11a (diamond symbols). The MS signals at $m/z = 18$ (Fig. 11c) were invariably identical whichever CO_2 composition was in place in the feed stream. In addition, the integrated areas under the current signals at $m/z = 44$ were more or less the same thus pointing to nearly composition-indifferent CO_2 consumption. This behavior appears coherent with carbonation of a Mg monolayer where only 2.5% of the total core Mg in chrysotile was used up before
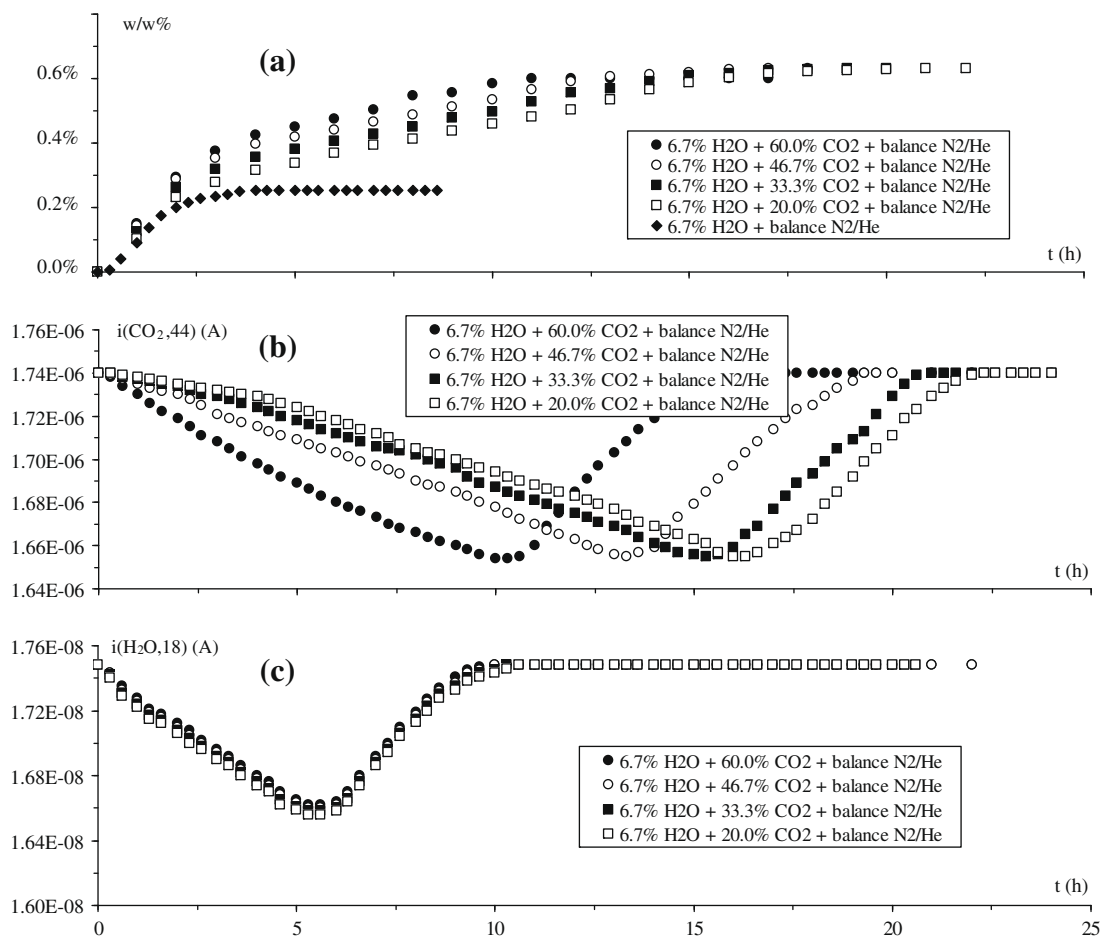
Fig. 11. Effect of CO_2 mole fraction in moist carbonation at 375 °C (a) net mass gain $W_{CO_2+H_2O}$ in w/w%, (b) corresponding positive ion currents at $m/z = 44$, (c) corresponding positive ion currents at $m/z = 18$. Diamond symbol in (a) mass gain w/w% H_2O due only to water under same temperature conditions in absence of CO_2. $P_{total} = 0.1$ MPa.

passivation by hydromagnesite would have blocked access to deeper core Mg atoms.

Keeping CO_2 feed mole fraction near 60% while increasing H_2O mole fraction from 2% to 10% (balance He/N_2 to 150 NmL/min) displays carbonation kinetics with ultimate total uptakes increasing as H_2O composition rose (Fig. 12a). The corresponding positive ion currents at $m/z = 44$ and $m/z = 18$ are shown in Fig. 12b and c. Finally, Fig. 13 shows the effect of H_2O mole fraction at 375 °C on water uptake in absence of CO_2 corresponding to the same water compositions as for Fig. 12. Water uptake in Fig. 13 increases with increasing H_2O mol fraction suggesting it is determining the increasing trend of $CO_2 + H_2O$ uptake during moist carbonation (Fig. 12a). Fig. 12c shows that H_2O uptake during moist carbonation increases with increasing water composition in accordance with the trend in Fig. 13. Interestingly, such increased water uptake promoted fixation of increased amounts of CO_2 as suggested by the widening of the dipping curves in Fig. 12b. This result confirms that water can play a role in stabilizing the carbonates in the form of hydrates such as hydromagnesite as evidenced in the XRPD patterns of Fig. 5c.

4.4.3. Stimulating CO_2 fixation using alkali-doped and/or chrysotile amorphisation

Chrysotile reactivity was also tentatively stimulated by impregnation with alkali metals as these are well known to yield (super)basic surfaces when loaded upon alkaline-earth metal oxide surfaces (Reddy and Smirniotis, 2004) or when ion-exchanged on zeolites such as Y zeolite (Díaz et al., 2008). However, it is worth being reminded that in practice, implementation of such a stimulation strategy must a priori address cost and ecological footprint analyses for sequestration with alkali-promoted chrysotile. The unloaded chrysotile resulted in the carbonation of nearly 15% of surface core Mg. After alkali stimulation, it was found that the average ratio [mol CO_2/mol total core Mg]$_{doped\ chrysotile}$/[mol CO_2/mol total core Mg]$_{raw\ chrysotile}$ was equal to 2.69 for Cs-promoted, 1.99 for K-promoted, 1.76 for Na-promoted, 1.37 for Li-promoted materials. This indicates an enhancement in the carbonation capacity of chrysotile in moist carbonation tests in the following order: Cs > K > Na > Li. Recall that the modified sorbents had a 10 wt% X/MgO mass ratio (X = Li, Na, K or Cs) corresponding to 0.03 (Cs), 0.10 (K), 0.18 (Na), and 0.58
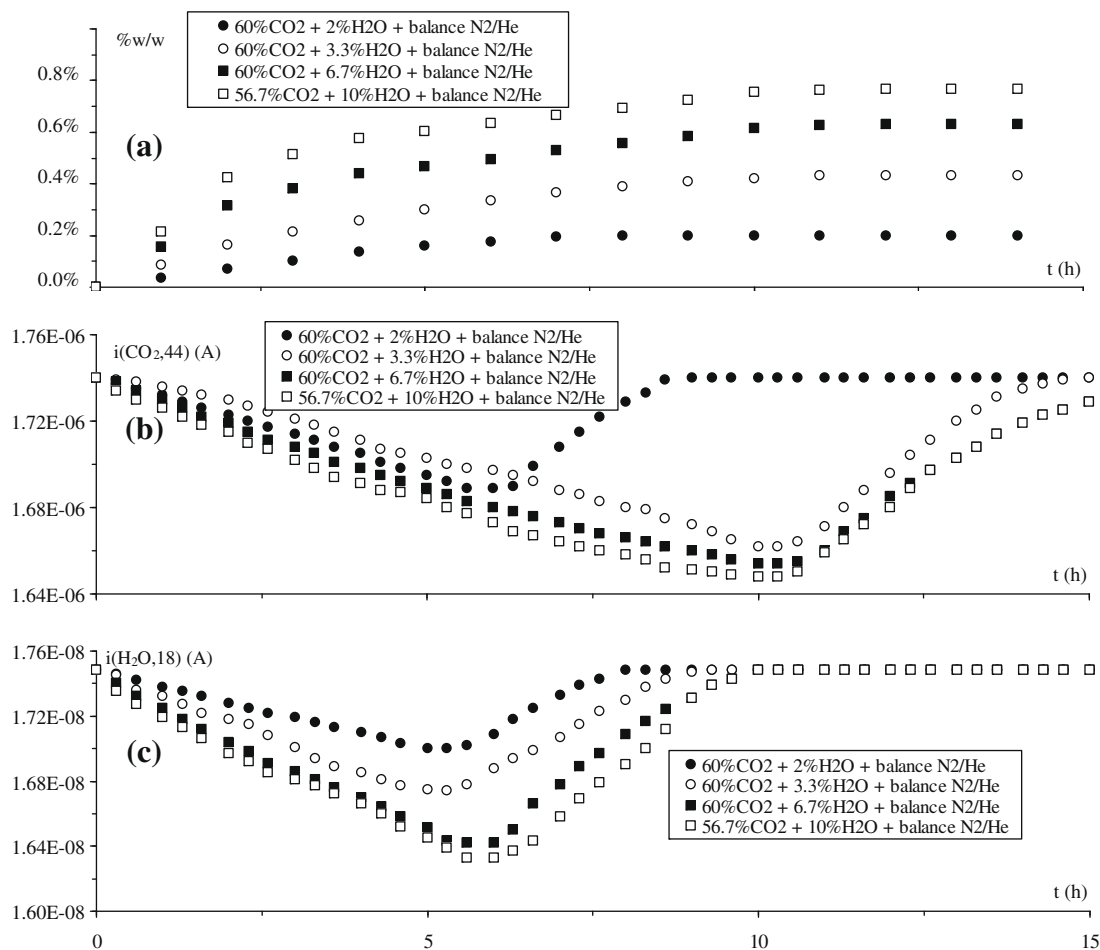
Fig. 12. Effect of H_2O mole fraction in moist carbonation at 375 °C (a) net mass gain $W_{CO_2+H_2O}$ in w/w%, (b) corresponding positive ion currents at $m/z = 44$, (c) corresponding positive ion currents at $m/z = 18$. $P_{total} = 0.1$ MPa.

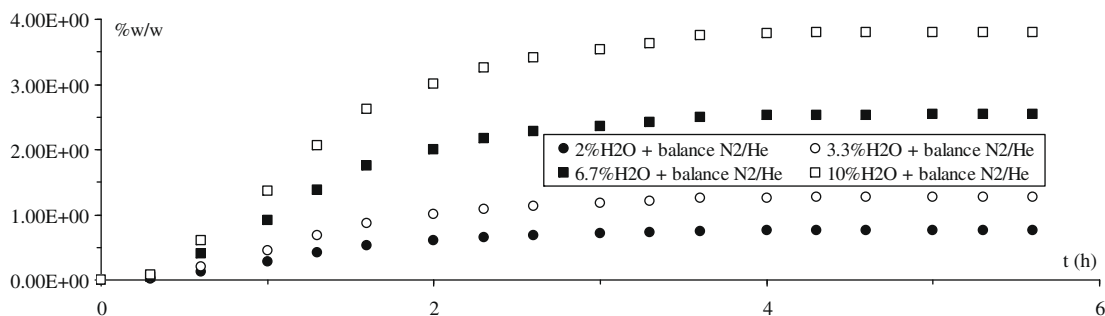Fig. 13. Effect of H_2O mole fraction at 375 °C on water uptake in absence of CO_2: mass gain W_{H_2O} in w/w% corresponding to water compositions of Fig. 12.

(Li) atom X/atom Mg. Therefore, the performance of the doped chrysotile has to be related more to the nature of the alkali elements rather than to their abundance. This trend seems more in line with the increased electropositivity of the doping element as the atomic number is increasing downwards from Li to Cs. After resting the water uptake, using Eqs. (3) and (4), Cs leads to the highest CO_2 uptake with an improvement in chrysotile carbonation by a factor

3 despite a reduction in initial BET surface area (Table 3) from 14.4 m²/g (bare chrysotile) to 8.2 m²/g (Cs-doped chrysotile). However, it is not evident that this enhancement is ascribable to promotion of chrysotile surface in the "catalytic" sense. At 375 °C, genuine CO_2 uptake increased from 2.5 wt% (Fig. 10b) to about 7.5 wt% after Cs impregnation (Fig. EA-1-7). With respect to reactive (core) Mg, a 9% Cs/Mg atom ratio was utilized for a
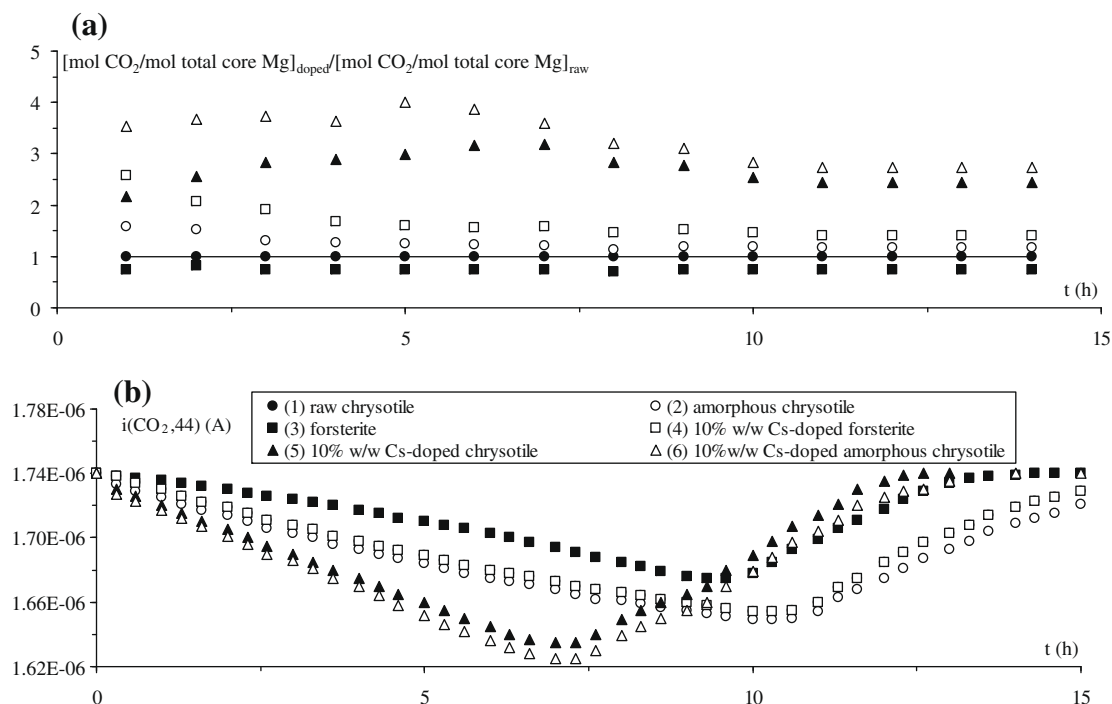
Fig. 14. Effect of crystalline magnesium silicate forms and Cs doping on CO_2 carbonation as normalized with respect to raw chrysotile: (1) raw chrysotile, (2) chrysotile fairly amorphised at 500 °C, (3) forsterite obtained after chrysotile calcination at 1000 °C, (4) Cs-doped forsterite, (5) Cs-doped chrysotile, (6) Cs-doped fairly amorphised chrysotile. (a) Time evolution of CO_2 mole fixation enhancement factor (expressed on a per total core Mg basis), (b) corresponding positive ion currents at $m/z = 44$. Moist carbonation at $T = 375$ °C, CO_2 (90 NmL/min)/H_2O (10 NmL/min)/balance He (50 NmL/min). $P_{total} = 0.1$ MPa.

10 wt% Cs/MgO mass ratio. Such 9% would result in 4.5% additional carbonation in the form of cesium carbonates had all of them been utilized. This gives 2.5% + 4.5%, i.e., 7 wt% which is comparable to the 7.5 wt% measured carbonation level. Considering the errors attached to these approximations along with the changing surface area, the promoting contribution of Cs remains difficult to constrain as crystalline cesium carbonates were not detected. However, the XPS studies (Fig. EA-1-3) suggest that cesium oxides can be carbonated.

Fig. 14 compares the carbonation capability of numerous chrysotile formulations with reference to raw chrysotile in moist carbonation at $T = 375$ °C. The moles of CO_2 molecules fixated per unit mol of total core Mg (Eq. (4)) have been used. Carbonation was followed for amorphised chrysotile at 500 °C, Cs-doped amorphised chrysotile at 500 °C, forsterite obtained after chrysotile calcination at 1000 °C, and Cs-doped forsterite. Forsterite carbonation was the less efficient; it was followed by raw chrysotile, amorphous chrysotile, Cs-doped forsterite, Cs-doped chrysotile, and then the best, Cs-doped amorphised chrysotile. However, in the latter case, the improvement with respect to the Cs-doped chrysotile was relatively minor. The CO_2 consumption dynamics exhibited by the different materials were also relatively diverse as suggested from the MS traces in Fig. 14b. Forsterite was kinetically the slowest and capacitively the smallest, while both Cs-doped chrysotile samples were kinetically the fastest and capacitively the largest (Fig. 14b).

Fig. 15 illustrates the dynamics in a series of cycles of successive moist carbonation at 375 °C and dry calcination 400 °C for bare and Cs-promoted chrysotile as a function of time for the total ($CO_2 + H_2O$) uptake. Each carbonation cycle lasted 26 h and was comprised of 14 h carbonation followed by 12 h calcination. Similarly the water uptake/drying cycles (no CO_2) lasted 14 h under humid stream and 12 h under dry inert stream. Water uptake dynamics in the absence of CO_2 is also shown for both materials. Chrysotile exhibited relatively reproducible fixation capacity with the progress of carbonation and calcination sequences. The calcination sequences subsequent to moist carbonation never retrieved the mass-less state of the pristine materials, unlike when only water was cycled.

4.5. Thermodynamic paths for gas–solid chrysotile carbonation at atmospheric pressure

In accordance with Lackner et al. (1995), the thermodynamic drive for serpentines to deep carbonation, reaction (R7) below, would have ceased at temperatures above 200 °C to the point the carbonation reaction kinetics, which requires higher temperatures, would have never become rapid. Furthermore, the arrangement of OH groups in the chrysotile structure suggests *core* and *lateral* Mg must dehydroxylate/carbonate following different elementary kinetic steps. This leans towards partial carbonation routes and formation of carbonates, other than $MgCO_3$, to be more favorable thermodynamically in the temperature range
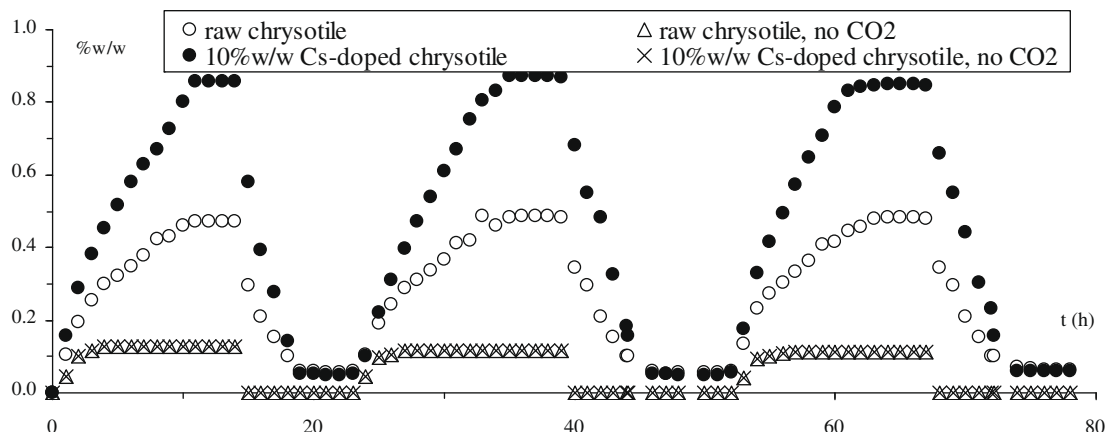
Fig. 15. Moist carbonation–dry calcination cycles of bare and Cs-promoted chrysotile as time evolution of total (CO_2 + H_2O) uptake. Water uptake dynamics in the absence of CO_2 is also shown for both materials. Moist carbonation at $T = 375$ °C, CO_2 (90 NmL/min)/H_2O (10 NmL/min)/balance He (50 NmL/min); dry calcination at $T = 400$ °C, N_2/He (150 NmL/min). $P_{total} = 0.1$ MPa.

where chrysotile carbonation was reactive in our tests ($T < 400$ °C) suggesting CO_2/Mg uptake ratios equal to 1/3, 1/6, and 4/15 rather than 1/1 as in (R7).
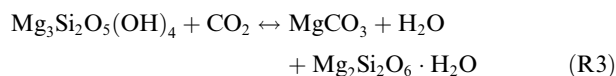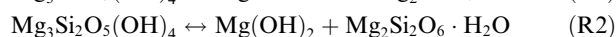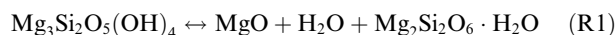
Making allowance of the high temperatures, the kinetics of these partial carbonation paths would be disrupted by passivating solid reaction products or by rapid sintering of reactive intermediates, thus possibly limiting conversion as observed in the TGA tested conditions (Fig. 10). Chrysotile dehydroxylation would also be adversely affected by kinetic effects associated with slowed down diffusion of H_2O molecules away from the dehydroxylating lattice sites as suggested by Béarat et al. (2002). Because of this effect, moist carbonation would have been less favorable than dry carbonation which is precisely the opposite of what our TGA/MS experimental observations revealed. Therefore, imposing water vapor compositions beyond the levels allowed by autogenous dehydroxylation is believed to also play a beneficial role in stabilizing the partially carbonated products in the form of $(MgCO_3)_x Mg(OH)_2 \cdot yH_2O$ (Fig. 5c).

Hereafter, products formation from the dry and moist carbonation of chrysotile is explained on thermodynamic grounds. The evolution as a function of temperature of the Gibbs free energies of the carbonation-related gas–solid reactions at 1 atm, involving CO_2, H_2O vapor, chrysotile, chrysotile proxies (e.g., periclase, brucite), and possible intermediates as well as end-products would allow one to identify some thermodynamic stability fields. The intermediate and end-products included in the analysis are magnesite ($MgCO_3$), silica (SiO_2), metastable dioctahedral chrysotile intermediate ($Mg_2Si_2O_6 \cdot H_2O$), clino-enstatite ($Mg_2Si_2O_6$), forsterite (Mg_2SiO_4), hydromagnesite (($MgCO_3$)$_4 Mg(OH)_2 \cdot$ $4H_2O$), artinite ($MgCO_3 Mg(OH)_2 \cdot 3H_2O$), and nesquehonite ($MgCO_3 \cdot 3H_2O$). Many of these latter hydrates are known to form in gentle hydrothermal conditions (Zhang et al., 2006) and are therefore likely to appear, at least as incipient phases, in our moist carbonation conditions.

The Gibbs free energies of formation of these species are from Robie and Hemingway (1995). When only the standard state is known, empirical ad hoc corrections of the temperature dependence have been assumed based on the T-dependence exhibited by compounds of similar struc-

tures. This was the case for hydromagnesite, artinite, and nesquehonite for which only standard-state data at 298 K are available (Robie and Hemingway, 1995; Königsberger et al., 1999). The postulated metastable dioctahedral chrysotile intermediate was assumed equivalent to the clino-enstatite (c-E) + water system. In addition, chrysotile being spatially inhomogeneous in its properties, it is not a pure compound in the phase rule sense (Evans, 2004). In this case, use was made in the thermodynamic calculations of the antigorite thermochemical data tabulated by Robie and Hemingway (1995). We have plotted $\Delta_r G^\circ(T, P = 1$ atm) where the Gibbs free energy change on reaction was evaluated with each species in its standard state (or state of unit activity), $G_i^\circ(T, P = 1$ atm, x_i°). The influence of CO_2 and H_2O mole fractions relevant to the TGA experimental conditions on the true Gibbs free energies, $\Delta_r G(T, P = 1$ atm), are also shown in the Electronic annex (Figs. EA-1-8 to EA-1-12).

Fig. 16a shows that monodehydroxylation of chrysotile (R1) into periclase (or brucite, (R2)) and dry chrysotile monocarbonation (R3) into magnesite would be thermodynamically feasible over nearly the same temperature domain where brucite dehydroxylation (R4) and periclase carbonation (R5) are reported to coincide at atmospheric conditions (Butt et al., 1996; Béarat et al., 2002; Lin et al., 2008). Thermodynamic feasibility of reactions (R1), (R2), (R3) in our reaction TGA conditions as performed at three typical compositions (total pressure = 0.1 MPa, $y_{H_2O} = 10^{-3}$, $y_{CO_2} = 0.67$ (balance = inert gas); $y_{H_2O} = 10^{-2}$, $y_{CO_2} = 0.66$ (balance = inert gas); and $y_{H_2O} = 10^{-1}$, $y_{CO_2} = 0.57$ (balance = inert gas)), see Figs. EA-1-8 and EA-1-9, is also confirmed.

$$Mg_3Si_2O_5(OH)_4 \leftrightarrow MgO + H_2O + Mg_2Si_2O_6 \cdot H_2O \quad (R1)$$

$$Mg_3Si_2O_5(OH)_4 \leftrightarrow Mg(OH)_2 + Mg_2Si_2O_6 \cdot H_2O \quad (R2)$$

$$Mg_3Si_2O_5(OH)_4 + CO_2 \leftrightarrow MgCO_3 + H_2O$$
$$+ Mg_2Si_2O_6 \cdot H_2O \quad (R3)$$

$$Mg(OH)_2 \leftrightarrow MgO + H_2O \quad (R4)$$

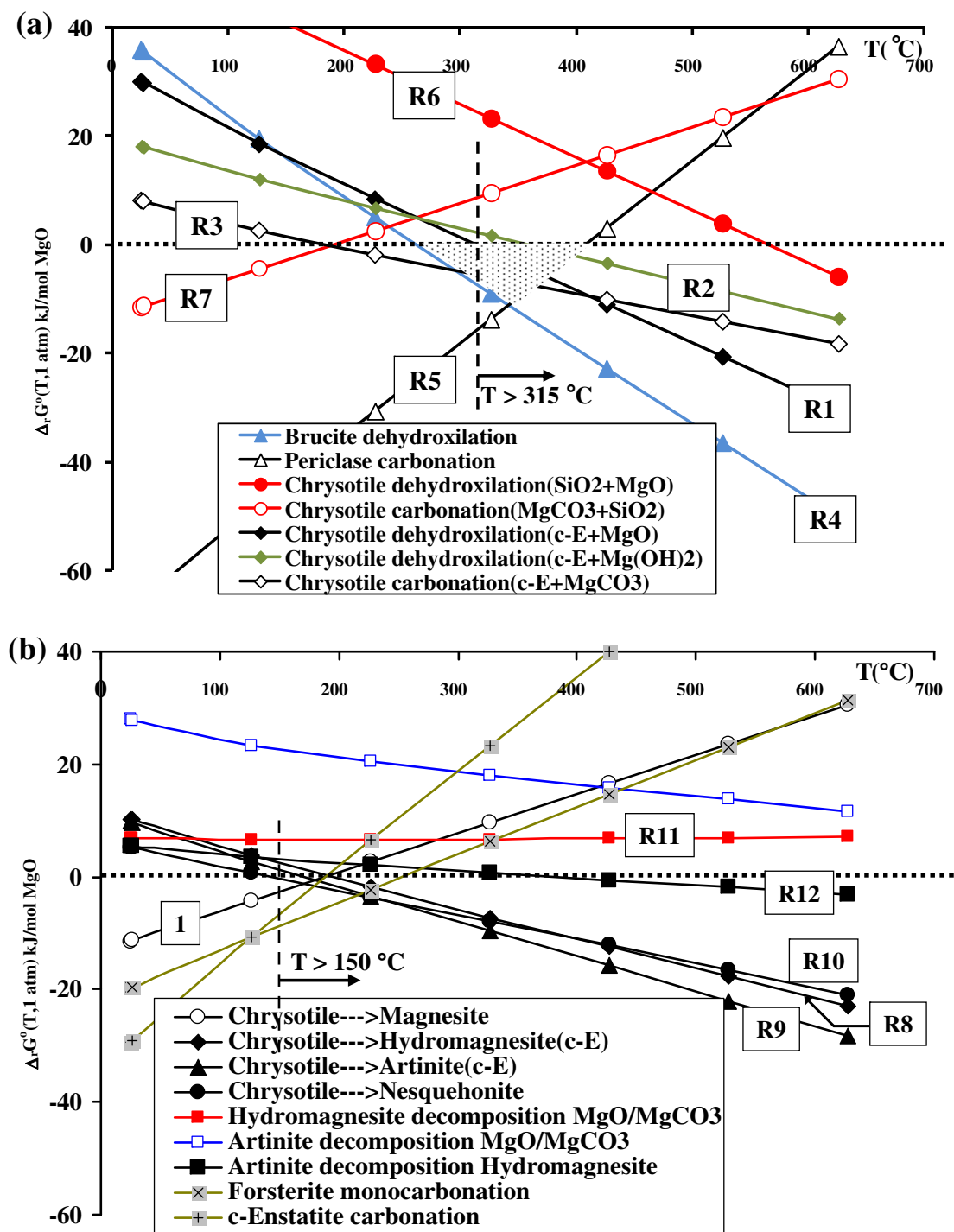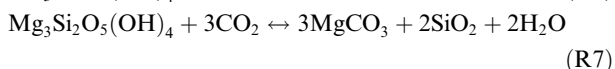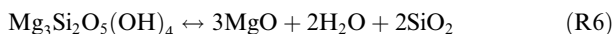$$MgO + CO_2 \leftrightarrow MgCO_3 \quad (R5)$$

Fig. 16. Evolution as a function of temperature of the reaction Gibbs free energies of (a) brucite dehydroxylation/carbonation, chrysotile partial (*c*-E route) and deep (SiO_2 route) dehydroxylation and ensuing partial and full dry carbonation, shaded area shows the thermodynamic region of feasibility for simultaneous dehydroxylation/carbonation of brucite (b) thermodynamic feasibility of chrysotile carbonation into magnesite, hydromagnesite, artinite and nesquehonite, of forsterite and *clino*-enstatite carbonation, and of hydromagnesite and artinite thermal decomposition into periclase/magnesite.

Conversely, Fig. 16a also illustrates the impossibility to delineate an overlap in the temperature ranges where deep dehydroxylation (R6) and deep dry carbonation

for chrysotile (R7) would cooperate as in the case of the brucite/periclase/magnesite system (shaded area in Fig. 16a):

$$Mg_3Si_2O_5(OH)_4 \leftrightarrow 3MgO + 2H_2O + 2SiO_2 \qquad (R6)$$

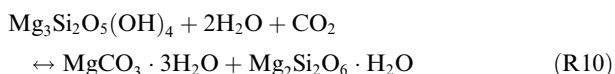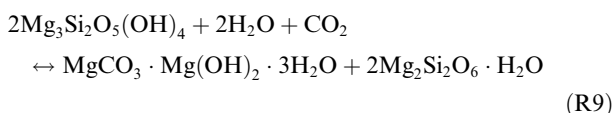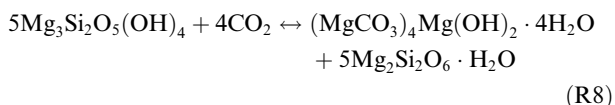$$Mg_3Si_2O_5(OH)_4 + 3CO_2 \leftrightarrow 3MgCO_3 + 2SiO_2 + 2H_2O \qquad (R7)$$

Although thermodynamically favorable at atmospheric pressure, dehydroxylation steps (R1), (R2), and (R6) are not that kinetically active below 600–650 °C (Cattaneo et al., 2003; Falini et al., 2004; Candella et al., 2007). This has led Lackner et al. (1995) to propose a two-step serpentine carbonation strategy with a high-temperature dehydroxylation step immediately followed by a lower-temperature step where carbonation reactivity of the metastable amorphous *para*-chrysotile could be enhanced. Béarat et al. (2002) proved the two-step feasibility in the case of brucite by inserting moist high-cooling rates between CO_2-deprived dehydroxylation and moist carbonation steps. Fagerlund et al. (2009) tested a three-step dehydroxylation/hydration/carbonation approach on Finnish lizardite/antigorite/chrysotile mixtures. The results consisted of net weight effects as the individual mass contributions of dehydroxylation and carbonation were difficult to disentangle. To circumvent the (R6):(R7) thermodynamic dilemma, other researchers (O'Connor et al., 2002; Park and Fan, 2004; McKelvy et al., 2004; Marato-Valer et al., 2005; Béarat et al., 2006; Gerdemann et al., 2007) turned away from gas–solid carbonation and opted for high-pressure high-temperature aqueous carbonation chemistries.

Very high-temperature thermal pre-treatments of chrysotile to allow its crystallization into forsterite and enstatite crystalline phases ($T > 700$ °C, Fig. 7a) have been shown to be inefficient (Fig. 14) as confirmed from their limited carbonation potential at 1 atm (Fig. 16b).

We have just identified reaction paths for partial carbonation of chrysotile that are thermodynamically feasible but yet kinetically not supported by our ex-situ observations nor by in-situ literature observations on dry dehydroxylation of chrysotile (Cattaneo et al., 2003; Candella et al., 2007) or its lizardite polymorph (McKelvy et al., 2004).

Fig. 16b shows that partial carbonation of chrysotile into hydromagnesite (R8), artinite (R9), and nesquehonite (R10) are thermodynamically plausible near the temperature range where chrysotile was observed to react. Thermodynamic feasibility of reactions (R8)–(R10) in our reaction TGA conditions as performed at three typical compositions (total pressure = 0.1 MPa, $y_{H_2O} = 10^{-3}$, $y_{CO_2} = 0.67$ (balance = inert gas); $y_{H_2O} = 10^{-2}$, $y_{CO_2} = 0.66$ (balance = inert gas) and $y_{H_2O} = 10^{-1}$, $y_{CO_2} = 0.57$ (balance = inert gas)) are also shown in Figs. EA-1-10 to EA-1-12.

$$5Mg_3Si_2O_5(OH)_4 + 4CO_2 \leftrightarrow (MgCO_3)_4Mg(OH)_2 \cdot 4H_2O + 5Mg_2Si_2O_6 \cdot H_2O \qquad (R8)$$

$$2Mg_3Si_2O_5(OH)_4 + 2H_2O + CO_2 \leftrightarrow MgCO_3 \cdot Mg(OH)_2 \cdot 3H_2O + 2Mg_2Si_2O_6 \cdot H_2O \qquad (R9)$$

$$Mg_3Si_2O_5(OH)_4 + 2H_2O + CO_2 \leftrightarrow MgCO_3 \cdot 3H_2O + Mg_2Si_2O_6 \cdot H_2O \qquad (R10)$$

Hydromagnesite decomposition (R11) once formed according to (R8) at TGA temperature conditions, seems improbable to occur during the cooling step preceding the ex-situ XRPD analyses:

$$(MgCO_3)_4Mg(OH)_2 \cdot 4H_2O \leftrightarrow 4MgCO_3 + MgO + 5H_2O \qquad (R11)$$
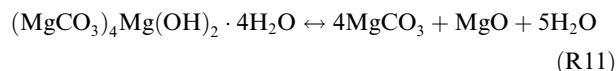
This result also appears to be supported by Botha and Strydom (2001) TGA experiments on dry hydromagnesite decomposition and who showed its relative reluctance to decompose in the temperature range up to 300 °C. The fact that a CO_2-rich atmosphere was maintained in our carbonation tests is believed to inhibit its decomposition at even higher temperatures as shown by Khan et al. (2001).

Artinite, if formed at TGA temperature conditions, could possibly decompose during cooling into hydromagnesite or less probably may split into periclase and magnesite:

$$H_2O + MgCO_3 \cdot Mg(OH)_2 \cdot 3H_2O + 3MgCO_3$$
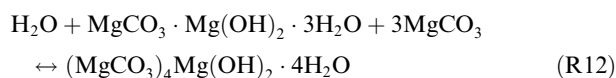$$\leftrightarrow (MgCO_3)_4Mg(OH)_2 \cdot 4H_2O \qquad (R12)$$

Fig. 16 shows that chrysotile reaction to magnesite is favored at low temperature but magnesite is not found in natural carbonation products of chrysotile milling residue. This is likely a consequence of a kinetic activation barrier preventing the spontaneous nucleation of magnesite. Our thermodynamic calculations yield slightly positive $\Delta_r G$ values for hydromagnesite (R8), nesquehonite (R10), and artinite (R9), that should indicate that this reaction is not possible at low temperature (<100 °C). The discrepancy between the thermodynamic calculation and the natural occurrence of surface weathering hydrated carbonates cementing chrysotile milling residue must indicate that some of the assumptions used to compute the Gibbs free energies are inaccurate at low temperature and that the Gibbs free energies for the reactions must be slightly negative. This gas–solid pathway has implications not only for mining residue carbon capture and storage but also for weathering of continental landmass and its major impact on the carbon cycle over geological time periods.

5. CONCLUDING REMARKS

The reaction between CO_2 (20–67 mol %) and chrysotile was studied at 0.1 MPa in dry and humid (up to 10 mol % of water) atmospheres between 300 and 1200 °C. The reaction was monitored using in-situ X-ray photoelectron spectroscopy (XPS), isothermal thermogravimetry/mass spectrometry, ex-situ X-ray powder diffraction (XRPD) and water and nitrogen adsorption/desorption. Humid carbonation was found to promote the conversion of chrysotile into crystalline magnesium carbonate hydrates (hydromagnesite). Crystalline magnesite went undetected irrespective of water composition of the gaseous stream. The highest carbon dioxide uptake was observed at 375 °C in moist atmosphere. A carbonate signature at 290.3 eV was identified via XPS on the surface of chrysotile subjected to humid carbonation. XRPD enabled us to assign these carbonate-bearing species to crystalline hydromagnesite that formed along with reaction-induced crystalline brucite. These results agree with

field observations that show that spontaneous carbonation under weathering conditions forms hydromagnesite within chrysotile milling residues in southern Québec. The studied gas–solid pathway has implications not only for mining residue carbon capture and storage but also for weathering of continental landmass and its major impact on the carbon cycle over geological time periods. Hydromagnesite was no longer discernable on the samples (both from XPS and XRPD) after calcination at 500 °C at the expense of marked peaks ascribed to crystalline periclase. A mechanistic speculation on chrysotile carbonation via monodehydroxylation of its brucitic (non-silicate attached) magnesium was proposed to explain the role of water in the carbonation reaction. A four-step carbonation mechanism was advanced to explain chrysotile reactivity: Step (1) chrysotile undergoes monodehydroxylation located on the brucitic magnesium; Step (2) a proton is transferred to the vacancy left by the exiting water; Step (3) (water-facilitated) intra-unit-cell rearrangement where a *lateral*-Mg hydroxyl group is re-composed and the amorphisation of the chrysotile intermediate is accelerated to free MgO; Step (4) water-stabilized $(MgCO_3)_x Mg(OH)_2 \cdot y H_2O$ hydrates are formed passivating the chrysotile surface along with possible water-facilitated sintering of $MgO/Mg(OH)_2$.

Chrysotile carbonation was slow at low pressure, which is interpreted in terms of incompatibility between CO_2 van der Waals molecular diameters and the narrow octahedral–tetrahedral lattice constants of chrysotile. It was estimated that at the optimal temperature (375 °C), nearly 15 atoms out of 100 of the surface chrysotile *brucitic* Mg moiety have been carbonated. This was equivalent to the carbonation of about 2.5 at. % of the total brucitic Mg moiety in chrysotile. The carbonation of brucite impurities coexisting in chrysotile was estimated to contribute by less than 17.6 at. % of the total converted magnesium. After alkali stimulation, it was found that the average ratio [mol CO_2/mol total core Mg]$_{doped\ chrysotile}$/[mol CO_2/mol total core Mg]$_{raw\ chrysotile}$ was equal to 2.69 for Cs-promoted (3 Cs atoms per 100 Mg atoms), 1.99 for K-promoted (10 K atoms per 100 Mg atoms), 1.76 for Na-promoted (18 Na atoms per 100 Mg atoms), 1.37 for Li-promoted (58 Li atoms per 100 Mg atoms) materials.

Preventive thermal pretreatments to amorphise chrysotile showed limited enhancement of carbonation capacity. A few crystalline magnesium silicates derived from chrysotile were also tested for carbonation: chrysotile amorphised at 500 °C, forsterite and Cs-stimulated forsterite were both obtained after chrysotile calcination at 1000 °C. Forsterite was kinetically the slowest and capacitively the smallest whereas the fastest and largest carbonation is measured for the Cs-doped chrysotile samples.

Our experiments were unlikely to have carbonated more than the outermost brucite-like chrysotile sheet exposed before reaction by the stacked nanofibril assemblages, and this despite the relative mobility of water molecules in and out during reaction, and in spite of partial amorphisation of the deeper magnesium sheets. Despite partial carbonation/ monodehydroxylation being possible thermodynamic paths, the low reaction extent stems from an accumulating hydromagnesite passivation layer atop the materials.

APPENDIX A. SUPPLEMENTARY DATA

Supplementary data associated with this article can be found, in the online version, at doi:10.1016/j.gca.2010.03. 007.

REFERENCES

Auzende A. L., Daniel I., Reynard B., Lemaire C. and Guyot F. (2004) High-pressure behaviour of serpentine minerals: a Raman spectroscopy study. *Phys. Chem. Miner.* **31**, 269–277.

Béarat H., McKelvy M. J., Chizmeshya A. W., Sharma R. and Carpenter R. W. (2002) Magnesium hydroxide dehydroxylation/carbonation reaction processes: implications for carbon dioxide mineral sequestration. *J. Am. Ceram. Soc.* **85**, 742–748.

Béarat H., McKelvy M. J., Chizmeshya A. W. G., Gormley D., Nunez R., Carpenter R. W., Squires K. and Wolf G. H. (2006) Carbon sequestration via aqueous olivine mineral carbonation: role of passivating layer formation. *Environ. Sci. Technol.* **40**, 4802–4808.

Beaudoin G., Hébert R., Constantin M., Duchesne J., Cecchi E., Huot F., Vigneau S. and Fiola R. (2008) Spontaneous carbonation of serpentine in milling and mining waste, southern Québec and Italy. Accelerated Carbonation for Environmental and Materials Engineering (ACEME2008), Rome, Italy, pp. 73–82.

Berner R. A. and Kothavala Z. (2001) GEOCARB III: a revised model of atmospheric CO_2 over Phanerozoic time. *Am. J. Sci.* **301**, 182–204.

Bernstein L. et al. (2007) *Climate change synthesis report: an assessment of the intergovernmental panel on climate change.* Available from: <http://www.ipcc.ch/pdf/assessment-report/ ar4/syr/ar4_syr.pdf>.

Botha A. and Strydom C. A. (2001) Preparation of a magnesium hydroxy carbonate from magnesium hydroxide. *Hydrometallurgy* **62**, 175–183.

Butt D. P., Lackner K. S., Wendt C. H., Conzone S. D., Kung H., Lu Y. C. and Bremser J. K. (1996) Kinetics of thermal dehydroxylation and carbonation of magnesium hydroxide. *J. Am. Ceram. Soc.* **79**, 1892–1898.

Candella P. A., Crummett C. D., Earnest D. J., Frank M. R. and Wylie A. G. (2007) Low-pressure decomposition of chrysotile as a function of time and temperature. *Am. Mineral.* **92**, 1704–1713.

Cattaneo A., Gualtieri A. F. and Artioli G. (2003) Kinetic study of the dehydroxylation of chrysotile asbestos with temperature by in situ XRPD. *Phys. Chem. Miner.* **30**, 177–183.

Chieh C. (2005) Fundamental characteristics of water. In *Handbook of Food Science, Technology, and Engineering*, vol. 1 (eds. Y. H. Hui, S. Duncan, I. Guerrero-Legarreta, E. C. Y. Li-Chan, C. H. Manley, W.-K. Nip, T. A. McMeekin, L. M. L. Nollet and M. Shafiur Rahman). CRC Press, Taylor and Francis, USA, pp. 12.1–12.17 (Chapter 12).

Díaz E., Muñoz E., Vega A. and Ordóñez S. (2008) Enhancement of the CO_2 retention capacity of Y-zeolites by Na and Cs treatments: effect of adsorption temperature and water treatment. *Ind. Eng. Chem. Res.* **47**, 412–418.

Dufaud F., Martinez I. and Shilobreeva S. (2009) Experimental study of Mg-rich silicates carbonation at 400 and 500 °C and 1 kbar. *Chem. Geol.* **265**, 79–87.

Evans B. W. (2004) The serpentinite multisystem revisited: chrysotile is metastable. In *Serpentine and Serpentinites: Mineralogy, Petrology, Geochemistry, Ecology, Geophysics, and Tectonics*, vol. 8 (ed. W. G. Ernest). International Book Series, Geological Society of America, Washington, D.C., USA, pp. 5–32.

Evans J. V. and Whateley T. L. (1967) Infra-red study of adsorption of carbon dioxide and water on magnesium oxide. *Trans. Faraday Soc.* **63**, 2769–2777.

Fagerlund J., Teir S., Nduagu E. and Zevenhoven R. (2009) Carbonation of magnesium silicate mineral using a pressurised gas/solid process. *Energy Procedia* **1**, 4907–4914.

Falini G., Foresti E., Gazzano M., Gualtieri A. F., Leoni M., Lesci I. G. and Roveri N. (2004) Tubular-shaped stoichiometric chrysotile nanocrystals. *Chem. Eur. J.* **10**, 3043–3049.

Gerdemann S. J., O'Connor W. K., Dahlin D. C., Penner L. R. and Rush H. (2007) Ex situ aqueous mineral carbonation. *Environ. Sci. Technol.* **41**, 2587–2593.

Giammar D. E., Bruant, Jr., R. G. and Peters C. A. (2005) Forsterite dissolution and magnesite precipitation at conditions relevant for deep saline aquifer storage and sequestration of carbon dioxide. *Chem. Geol.* **217**, 257–276.

Goel N. (2006) In situ methane hydrate dissociation with carbon dioxide sequestration: current knowledge and issues. *J. Petrol. Sci. Eng.* **51**, 169–184.

Gollmann M. A. C., Capeletti L. B., Fisch A. G., dos Santos J. H. Z. and Miranda M. S. L. (2008) Adsorbents for acetone in cyclohexane effluent employed in Ziegler–Natta catalyst process. *Adsorption* **14**, 805–813.

Gollmann M. A. C., Capeletti L. B., Miranda M. S. L. and dos Santos J. H. Z. (2009) Modified sorbents for acetone adsorption: application in ethylene polymerization process. *Chem. Eng. J.* **147**, 383–390.

Gruszkiewicz M. S., Horita J., Simonson J. M., Mesmer R. E. and Hulen J. B. (2001) Water adsorption at high temperature on core samples from the Geysers geothermal field, California, USA. *Geothermics* **30**, 269–302.

Hamoudi S., Larachi F., Adnot A. and Sayari A. (1999) Characterization of spent MnO_2/CeO_2 wet oxidation catalyst by TPO–MS, XPS, and S-SIMS. *J. Catal.* **185**, 333–344.

Huot F., Beaudoin G., Hébert R., Constantin M., Bonnin G. and Dipple D. M. (2003) Evaluation of Southern Québec (Canada) serpentine mine residues for CO_2 sequestration by mineral carbonation: preliminary results. In *Second Annual Conference on Carbon Sequestration*, Alexandria, Virginia, USA.

Jolicoeur C., Roberge P. and Fortier J. L. (1981) Separation of short fibers from bulk chrysotile asbestos fiber materials: analysis and physico-chemical characterization. *Can. J. Chem.* **59**, 1140–1148.

Kalinichenko E. A. and Litovchenko A. S. (2000) Effect of an electric field on brucite dehydroxylation. *Phys. Solid State* **42**, 2070–2075.

Khan N., Dollimore D., Alexander K. and Wilburn F. W. (2001) The origin of the exothermic peak in the decomposition of basic magnesium carbonate. *Thermochim. Acta* **367–368**, 321–333.

Königsberger E., Königsberger L. C. and Gamsjäger H. (1999) Low-temperature thermodynamic model for the system $Na_2CO_3–MgCO_3–CaCO_3–H_2O$. *Geochim. Cosmochim. Acta* **63**, 3105–3119.

Krevor S. C. and Lackner K. S. (2009) Enhancing process kinetics for mineral carbon sequestration. *Energy Procedia* **1**, 4867–4871.

Krinari G. A. and Khalitov Ya. Z. (1995) Defects in crystalline structure of chrysotile and their role in development of technological properties of asbestos fiber. *J. Mining Sci.* **31**, 314–320.

Lackner K. S. (2003) A guide to CO_2 sequestration. *Science* **300**, 1677–1678.

Lackner K. S., Wendt C. H., Butt D. P., Joyce, Jr., E. L. and Sharp D. H. (1995) Carbon dioxide disposal in carbonate minerals. *Energy* **20**, 1153–1170.

Lackner K. S., Butt D. P. and Wendt C. H. (1997) Progress on binding CO_2 in mineral substrates. *Energy Convers. Manag.* **38**, S259–S264.

Larachi F., Dehkissia S., Adnot A. and Chornet E. (2004) X-ray photoelectron spectroscopy, photoelectron energy loss spectroscopy, X-ray excited Auger electron spectroscopy, and time-of-flight-secondary ion mass spectroscopy studies of asphaltenes from Doba-Chad heavy crude hydrovisbreaking. *Energy Fuels* **18**, 1744–1756.

Li Y., Liu Y., Wang Y., Leng Y., Xie L. and Li X. (2007) Hydrogen storage properties of $[M(Py)\{Ni(CN)4\}]$ (M = Fe, Co, Ni). *Int. J. Hydrogen Energy* **32**, 3411–3415.

Lin P. C., Huang C. W., Hsiao C. T. and Teng H. (2008) Magnesium hydroxide extracted from a magnesium-rich mineral for CO_2 sequestration in a gas–solid system. *Environ. Sci. Technol.* **42**, 2748–2752.

Liu K., Feng Q., Yang Y., Zhang G., Ou L. and Lu Y. (2007) Preparation and characterization of amorphous silica nanowires from natural chrysotile. *J. Non-Cryst. Solids* **353**, 1534–1539.

Mamontov E., Kumzerov Yu. A. and Vakhrushev S. B. (2005) Translational dynamics of water in the nanochannels of oriented chrysotile asbestos fibers. *Phys. Rev. E* **71**, 061502.

Marato-Valer M. M., Fauth D. J., Kuchta M. E., Zhang Y. and Andrésen J. M. (2005) Activation of magnesium rich minerals as carbonation feedstock materials for CO_2 sequestration. *Fuel Process. Technol.* **86**, 1627–1645.

McKelvy M. J., Sharma R., Chizmeshya A. V. G., Carpenter R. W. and Streib K. (2001) Magnesium hydroxide dehydroxylation: in situ nanoscale observation of lamellar nucleation and growth. *Chem. Mater.* **13**, 921–926.

McKelvy M. J., Chizmeshya A. V. G., Diefenbacher J., Béarat H. and Wolf G. (2004) Exploration of the role of heat activation in enhancing serpentine carbon sequestration reactions. *Environ. Sci. Technol.* **38**, 6897–6903.

Nahdi K., Rouquerol F. and Ayadi M. T. (2009) $Mg(OH)_2$ dehydroxylation: a kinetic study by controlled rate thermal analysis (CRTA). *Solid State Sci.* **11**, 1028–1034.

O'Connor W. K., Dahlin D. C., Rush G. E., Dahlin C. L. and Collins W. K. (2002) Carbon dioxide sequestration by direct mineral carbonation: process mineralogy of feed and products. *Miner. Metall. Process.* **19**, 95–101.

O'Connor W. K., Dahlin D. C., Rush G. E., Gerdemann S. J., Penner L. R. and Nilsen D. N. (2005) Aqueous mineral carbonation, mineral availability, pretreatment, reaction, parametrics, and process studies. DOE/ARC-TR-04-002, Final report, March 2005, 491 pp.

Park A. H. A. and Fan L. S. (2004) CO_2 mineral sequestration: physically activated dissolution of serpentine and pH swing process. *Chem. Eng. Sci.* **59**, 5241–5247.

Philipp R. and Fujimoto K. (1992) FTIR spectroscopic study of CO_2 adsorption/desorption on MgO/CaO catalysts. *J. Phys. Chem.* **96**, 9035–9038.

Piché S. and Larachi F. (2005) Degradability of iron(III)-aminopolycarboxylate complexes in alkaline media: statistical design

and X-ray photoelectron spectroscopy studies. *Ind. Eng. Chem. Res.* **44**, 5053–5062.

Reddy E. P. and Smirniotis P. G. (2004) High-temperature sorbents for CO_2 made of alkali metals doped on CaO supports. *J. Phys. Chem. B* **108**, 7794–7800.

Robie R. A. and Hemingway B. S. (1995) *Thermodynamic properties of minerals and related substances at 298.15 K and 1 bar (10^5 pascals) pressure and at higher temperatures.* U.S. Geological Survey Bulletin, No. 2131.

Schulze R. K., Hill M. A., Field R. D., Papin P. A., Hanrahan R. J. and Byler D. D. (2004) Characterization of carbonated serpentine using XPS and SEM. *Energy Convers. Manag.* **45**, 3169–3179.

Seifritz W. (1990) CO_2 disposal by means of silicates. *Nature* **345**, 486.

Teir S., Eloneva S., Fogelholm C. J. and Zevenhoven R. (2009) Fixation of carbon dioxide by producing hydromagnesite from serpentinite. *Appl. Energy* **86**, 214–218.

Thomassin J. H., Goni J., Baillif P., Touray J. C. and Jaurand M. C. (1977) An XPS study of the dissolution kinetics of chrysotile in 0.1 N oxalic acid at different temperatures. *Phys. Chem. Miner.* **1**, 385–398.

Turci F., Tomatis M., Mantegna S., Cravotto G. and Fubini B. (2008) A new approach to the decontamination of asbestos-polluted waters by treatment with oxalic acid under power ultrasound. *Ultrason. Sonochem.* **15**, 420–427.

Wagner C. D., Naumkin A. V., Kraut-Vass A., Allison J. W., Powell C. J. and Rumble, Jr., J. R. (2007) NIST X-ray Photoelectron Spectroscopy Database, NIST Standard Reference Database 20, Version 3.5. Available from: <http://srdata.nist.gov/xps/>.

Whittaker E. J. W. (1956a) The structure of chrysotile. II. Clino-chrysotile. *Acta Crystallogr.* **9**, 855–861.

Whittaker E. J. W. (1956b) The structure of chrysotile. III. Ortho-chrysotile. *Acta Crystallogr.* **9**, 862–864.

Whittaker E. J. W. (1956c) The structure of chrysotile. IV. Para-chrysotile. *Acta Crystallogr.* **9**, 865–867.

Wilson S. A., Dipple G. M., Powe I. M., Thom J. M., Anderson R. G., Raudsepp M., Gabites J. E. and Southam G. (2009) Carbon dioxide fixation within mine wastes of ultramafic-hosted ore deposits: examples from the Clinton Creek and Cassiar chrysotile deposits, Canada. *Econ. Geol.* **104**, 95–112.

Zevenhoven R. and Kohlmann J. (2001) CO_2 sequestration by magnesium silicate mineral carbonation in Finland. In *Second Nordic Minisymposium on Carbon Dioxide Capture and Storage*, Göteborg, October 26. Available from: <http://www.entek.-chalmers.se/~anly/symp/symp2001.html>.

Zevenhoven R., Eloneva S. and Teir S. (2006) Chemical fixation of CO_2 in carbonates: routes to valuable products and long-term storage. *Catal. Today* **115**, 73–79.

Zevenhoven R., Teir S. and Eloneva S. (2008) Heat optimisation of a staged gas–solid mineral carbonation process for long-term CO_2 storage. *Energy* **33**, 362–370.

Zhang Z., Zheng Y., Ni Y., Liu Z., Chen J. and Liang X. (2006) Temperature and pH-dependent morphology and FT-IR analysis of magnesium carbonate hydrates. *J. Phys. Chem. B* **110**, 12969–12973.

Associate editor: Roy A. Wogelius